



## RESEARCH ARTICLE

10.1002/2015JF003794

## Key Points:

- Mobile armors can be characterized in terms of an equilibrium bed structure
- Mobile armor structure is not sensitive to the formative transport rate except when rates are low
- Isolating different scales of topographic variation is important when interpreting surface metrics

## Correspondence to:

D. M. Powell,  
dmp6@leicester.ac.uk

## Citation:

Powell, D. M., A. Ockelford, S. P. Rice, J. K. Hillier, T. Nguyen, I. Reid, N. J. Tate, and D. Ackerley (2016), Structural properties of mobile armors formed at different flow strengths in gravel-bed rivers, *J. Geophys. Res. Earth Surf.*, 121, doi:10.1002/2015JF003794.

Received 18 NOV 2015

Accepted 24 JUL 2016

Accepted article online 29 JUL 2016

## Structural properties of mobile armors formed at different flow strengths in gravel-bed rivers

D. Mark Powell<sup>1</sup>, Annie Ockelford<sup>2</sup>, Stephen P. Rice<sup>3</sup>, John K. Hillier<sup>3</sup>, Thao Nguyen<sup>1</sup>, Ian Reid<sup>3</sup>, Nicholas J. Tate<sup>1</sup>, and David Ackerley<sup>1</sup>

<sup>1</sup>Department of Geography, University of Leicester, Leicester, UK, <sup>2</sup>School of Environment and Technology, University of Brighton, Brighton, UK, <sup>3</sup>Department of Geography, Loughborough University, Loughborough, UK

**Abstract** Differences in the structure of mobile armors formed at three different flow strengths have been investigated in a laboratory flume. The temporal evolution of the bed surfaces and the properties of the final beds were compared using metrics of surface grain size, microtopography, and bed organization at both grain and mesoscales. Measurements of the bed condition were obtained on nine occasions during each experiment to describe the temporal evolution of the beds. Structured mobile armors formed quickly in each experiment. At the grain scale (1–45 mm;  $9 \leq D_{50} \leq 17$  mm where  $D_{50}$  is the median surface particle size), surface complexity decreased and bed roughness increased in response to surface coarsening and the development of the mobile armor. Particles comprising the armor also became flow aligned and developed imbrication. At a larger scale (100–200 mm), the surface developed a mesoscale topography through the development of bed patches with lower and higher elevations. Metrics of mobile armor structure showed remarkable consistency over prolonged periods of near-constant transport, demonstrating for the first time that actively transporting surfaces maintain an equilibrium bed structure. Bed structuring was least developed in the experiments conducted at the lowest flow strength. However, little difference was observed in the structural metrics of the mobile armors generated at higher flows. Although the range of transport rates studied was limited, the results suggest that the structure of mobile armors is insensitive to the formative transport rate except when rates are low ( $\tau^* \approx 0.03$  where  $\tau^*$  is the dimensionless shear stress).

### 1. Introduction

The bed surface of an alluvial river is the primary interface between the flow of water and the sediment available for transport. As such, it is a critical component of the fluvial system, exerting a fundamental influence on near-bed hydraulics [Hardy *et al.*, 2010], resistance to flow [Powell, 2014], and sediment transport rate and grain-size distribution [Gomez, 1995]. Moreover, as a result of feedbacks between the bed, the flow, and the transported sediment, the channel bed is free to adjust to changes in discharge [Parker *et al.*, 2003] and sediment supply [Dietrich *et al.*, 1989]. It thus represents a potential degree of freedom in river self-organization and adjustment [Ferguson, 2008; Ferguson *et al.*, 2015].

Conventionally, the surfaces of gravel-bed rivers are described and characterized by particle size and, as a result, there is a large literature concerning sampling techniques and standards for determining particle size characteristics of streams and rivers [e.g., Bunte and Abt, 2001]. However, river bed roughness and stability cannot simply be attributed to particle size because the development of bed structure—variations in the spacing, packing, and geometrical arrangement of particles [Laronne and Carson, 1976]—evolves concurrently with armoring as particles in traction come to rest in stable positions, often against other stable particles. Recognizable particle configurations tend to develop, reflecting the arrangement of individual particles, for example, alignment or imbrication [Johansson, 1976; Qin *et al.*, 2012], and the organization of particles into coherent bed forms such as pebble clusters [Brayshaw, 1984] and stone cells [Church *et al.*, 1998]. There is a growing understanding of how different bed structures contribute to bed roughness and stability through the generation of turbulence [Lacey and Roy, 2008; Papanicolaou *et al.*, 2001; Hardy *et al.*, 2010; Tan and Curran, 2012; Curran and Tan, 2014], the promotion of form drag [Hassan and Reid, 1990; Clifford *et al.*, 1992; Hassan and Church, 2000], modifications to particle exposure and grain pivot angles [Kirchner *et al.*, 1990; Hodge *et al.*, 2013], and the spatial distribution of cluster forms [Piedra *et al.*, 2012]. However, relatively little is known about the factors that are conducive to the development of bed structures in gravel-bed rivers and whether different conditions promote the development of different types or degrees of bed structuring.

©2016. The Authors.

This is an open access article under the terms of the Creative Commons Attribution License, which permits use, distribution and reproduction in any medium, provided the original work is properly cited.

Differences between the structural characteristics of screeded and water-worked gravel beds have been attributed to the development of streambed armors [Nikora *et al.*, 1998; Cooper and Tait, 2009]. Several workers have reported the results of flume experiments showing the simultaneous development of bed structures and static armors (those formed under conditions of zero sediment flux; Church *et al.* [1998]). Under these conditions, the structural properties of static armors have been related to the armoring discharge [Aberle and Nikora, 2006] and the proportion of sand in the bulk sediment mixture [Curran and Waters, 2014]. Other workers have considered the structural properties of mobile armors formed under a variety of upstream sediment supply conditions [e.g., Hassan and Church, 2000; Marion *et al.*, 2003] and have highlighted some differences with the static armor case. Mao *et al.* [2011], for example, found that static and mobile armors differed in their response to increasing discharge: static armors displayed limited variation in vertical roughness scale and became less topographically complex whereas mobile armors exhibited increased roughness length scales, less organization, and larger cluster structures. The differences were attributed to the active transport and greater protrusion of coarse bed material in the mobile armor case. The literature also suggests that bed surface structure should be influenced by sediment sorting. Reid *et al.* [1992] and Wittenberg [2002], for example, report field results that demonstrate that the occurrence of pebble clusters increases as bed material sorting decreases (i.e., as sorting indices increase), and Church *et al.* [1998] note that bed structures are rarely reported in flume studies using narrowly graded sediments. This is counter to Strom *et al.* [2004], who recorded the development of pebble clusters in uniform sediments in their flume experiments. Other workers have stressed hydrological controls. Wittenberg [2002] found that the density of pebble clusters was lower in dryland ephemeral rivers than in humid-temperate perennial rivers and attributed the difference to the flashy discharge regime and absence of base flow in dryland channels, which restricts the period for cluster development. The importance of flow regime is supported by the work of Haynes and Pender [2007] and Ockelford and Haynes [2013], who demonstrate significant changes to packing arrangements and particle orientations during the periods of subthreshold flows between competent flow events, and by Mao [2012], who documented time-dependent variations in bed structure during the passage of stepped hydrographs. Other studies suggest that a temporal dimension to bed structural development may exist. Increases in bed roughness with flow duration have been attributed to structure development, as well as bed surface grain-size changes, by Pender *et al.* [2001], Marion *et al.* [2003], Mao *et al.* [2011], and Ockelford and Haynes [2013], and Marion *et al.* [2003] have further shown that different bed structures can form over different timescales.

In this paper, we report on a series of mobile-bed laboratory flume experiments designed to quantify the effect of sediment transport rate on the development of bed surface structure in gravel-bed rivers. Most of the studies referred to above concentrate on describing the structural properties of equilibrium channel beds and as a result, they sample the bed relatively infrequently. A novel aspect of this study is the adoption of a high sampling frequency in an explicit attempt to capture the evolution of gravel-bed structure as equilibrium bed conditions develop. Another innovation is the use of a regional-residual separation technique to isolate different components of the bed surface topography; specifically the contributions made at mesoscale and grain scale. The primary goals of the paper are to: (1) describe and account for the structural characteristics of mobile armors formed in a laboratory flume; (2) quantify the evolution of mobile armor structure from an initial, screeded, bed surface condition; and (3) explore how mobile armor structure is influenced by transport rate.

## 2. Experimental Methods

### 2.1. Overview

Three flume experiments (e1–e3) were conducted with a sediment recirculation protocol to compare the temporal evolution and surface properties of mobile armors formed at different flow strengths. Each experiment was repeated once (e1r–e3r) to assess the replicability of the experiments. The flows were designed using the concept of transport intensity,  $\tau^*/\tau_c^*$ , where  $\tau^*$  is the dimensionless shear stress and  $\tau_c^*$  the value of  $\tau^*$  at the threshold of motion, which is typically low in most gravel-bed rivers, even at bank full flow ( $\tau^*/\tau_c^* \leq 1.6$ ; [Parker, 2006]). In this study, different flow strengths were generated by keeping the flow depth constant and varying the flume slope. We selected the slope of each experiment to generate a range of representative transport intensities under the assumption that  $\tau_c^* = 0.03$ , a value that is toward the lower end of estimates published in the literature [Buffington and Montgomery, 1997; Petit *et al.*, 2015] but typical of bed surface conditions that develop in laboratory flumes at low  $\tau^*$  [Ferguson, 2012]. The experimental sediment comprised a mixture of fluvial sands and gravels. The development of the bed surface condition was evaluated at the beginning and

**Table 1.** Experimental Conditions<sup>a</sup>

Experiment	Bulk Sediment			Flow Conditions		Initial Experimental Parameters <sup>b</sup>				Final Experimental Parameters <sup>c</sup>			
	$D_{b16}$ , $D_{b84}$ , (mm)	$D_{b50}$ , (mm)	$\sigma_b$	$S$ ( $\text{mm}^{-1}$ )	$\tau$ ( $\text{N m}^{-2}$ ) <sup>d</sup>	$D_{s50}$ ( $D_{s84}$ ) (mm)	$\sigma_s$	$\tau^*$	$i_b$ ( $\text{g m}^{-1} \text{s}^{-1}$ )	$D_{s50}$ ( $D_{s84}$ ) (mm)	$\sigma_s$	$\tau^*$	$i_b$ ( $\text{g m}^{-1} \text{s}^{-1}$ )
e1				0.006	5.0	9.9 (19.7)	1.1	0.031	24.0	12.5 (22.5)	1.0	0.024	0.23
e1r	2.7					9.0 (20.8)	1.2	0.034	16.1	13.5 (25.4)	0.9	0.023	0.34
e2	8.3	1.5		0.009	7.4	9.4 (19.2)	1.1	0.049	51.5	16.1 (26.5)	0.9	0.029	1.02
e2r	23.0					10.7 (28.4)	1.3	0.043	39.2	16.3 (31.2)	1.1	0.028	1.19
e3				0.015	12.4	8.7 (19.6)	1.2	0.088	79.3	17.2 (33.6)	1.0	0.045	1.2
e3r						9.1 (18.9)	1.1	0.084	91.3	16.4 (26.6)	1.1	0.047	1.60

<sup>a</sup> $D_{bx}$  and  $D_{sx}$  are the xth percentiles of the bulk experimental mixture and bed surface grain-size distribution respectively,  $\sigma_b$  and  $\sigma_s$  are the sorting coefficients for the bulk experimental mixture and bed surface respectively,  $S$  is flume slope,  $\tau$  and  $\tau^*$  are the dimensional and dimensionless bed shear stress respectively and  $i_b$  is sediment transport rate.

<sup>b</sup>Measured at  $t = 0$  min except the initial transport rate which is sampled at  $t = 10$  min.

<sup>c</sup>Measured at  $t = 1200$  min except for experiment e3r where  $t = 900$  min.

<sup>d</sup>Corrected for sidewall effects using the method of Williams [1970].

end of each experiment and at seven time points during the experiments using measurements of surface grain size and topography. Bed load transport rates were also measured by periodically sampling the sediment exiting the flume. Table 1 provides a summary of the test conditions for the three treatments that made up the experimental program. Note that no data on the final bed surface condition is available for experiment e3r and that this experimental run, therefore, is truncated at the preceding sample interval ( $t = 900$  min where  $t$  is the elapsed time of the experiment).

## 2.2. Experimental Configuration

Experiments were performed within a glass-sided, 8.2 m long, flow-recirculating flume of rectangular cross section ( $0.6 \text{ m} \times 0.5 \text{ m}$ ). To prevent scour and to induce turbulent boundary conditions at the flume entrance, 2.1 m of immobile sediment was placed directly downstream of the water inlet. No measurements were made in the final 1.7 m of the flume in order to avoid drawdown effects. The flume, therefore, had an effective working length of 4.4 m which was covered with thoroughly mixed mobile test sediment to a depth of 90 mm (equivalent to  $\sim 11 D_{b50}$  and  $\sim 4D_{b84}$ , where  $D_{bx}$  is the xth percentile of the bulk experimental sediment mixture) which were screeded flat so the sediment surface was parallel to the flume floor.

The sediment mixture was made up from natural quartz-density river sands and gravels ranging between 1 and 45 mm in diameter. The sediment was sieved into 1/2 phi size fractions and recombined into a grain-size distribution with an inclusive graphic sorting coefficient ( $\sigma_b$ ) of 1.5 [Folk and Ward, 1957] and  $D_{b50}$  of 8 mm (Figure 1). The size distribution of the sediment mixture was not directly scaled from field samples, but the sorting value is representative of the lower limit of values found in 148 subsurface grain-size distributions from nine gravel-bed rivers, including Fraser, Sukunka, and Peace Rivers and Carnation Creek (Canada); Colorado River and Redwood Creek (USA); Drôme River (France), Ngaruroro River (New Zealand); and the River Wharfe, UK. These grain-size distributions were collected by us or were provided by colleagues (see acknowledgments). For these samples from predominantly large, piedmont, rivers with a riffle-pool style, the median sorting coefficient was 2.58 and the fifth percentile was 1.56, such that the degree of sorting in the sediment mixture used here falls in the lower tail of the natural distribution (since the proportion of the field grain-size distributions  $< 1$  and  $> 45$  mm were, on average, similar (cf. 0.15), the experimental mixture was not truncated more at one end of the grain-size distribution than the other). The well-sorted sediment helps to isolate sediment transport rate as the dominant treatment factor in the experiments, given the potential increase in structural development as sorting decreases [e.g., Reid et al., 1992]. Following Wilcock and McArdeil [1993], all the grains in each size fraction were painted a specific color so that surface grain-size distributions could be determined by counting the numbers of differently colored particles exposed on photographs of the bed.

A rigid tray ( $1000 \times 400 \text{ mm}$ ), formed from 8 mm thick stainless steel, was buried in the test sediments with its upstream edge 3 m from the flume inlet. The tray allowed removal of a portion of the bed, the test section, to facilitate measurements of surface topography, which were made outside the flume. Great care was taken when draining and refilling the flume and removing and replacing the test section so that disturbance to the bed surface was minimized, both inside and outside of the tray. At each sample interval, the pump

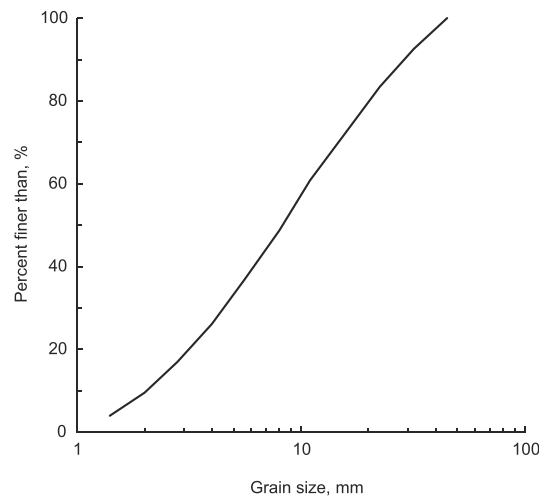


**Figure 1.** Grain-size distribution of the experimental sediment.

Measurement of bed surfaces in this manner has successfully been used before [Marion *et al.*, 2003; Cooper *et al.*, 2008; Ockelford and Haynes, 2013]. Refilling the flume was undertaken carefully with the bed flooded slowly before discharge was increased to the required level.

Flow depth ( $Y$ ) was set at 120 mm throughout each experiment to maintain a width:depth ratio of 5, thereby limiting the development of secondary flow cells [McLelland *et al.*, 1999]. The relative roughness ( $Y/D_{84}$ ) of the experimental mixture was 5.2 and, therefore, at the lower end of values that are typically observed in gravel-bed rivers ( $Y/D_{84} > 5$ ; [Bathurst, 1993]). Experiments were conducted at three slopes ( $S = 0.006, 0.009,$  and  $0.015$ ) which generated sidewall-corrected, dimensionless shear stress values ( $\tau^*$ ) for the initial ( $t = 0$  min) sediment surfaces of between 0.031 and 0.088 (Table 1;  $1.0 \leq \tau^*/\tau_c^* \leq 2.93$ ; sidewall correction after Williams [1970]). Equivalent values for the final surfaces ( $t = 1200$  min; Table 1) were slightly lower as a result of surface coarsening and ranged from 0.023 to 0.047 ( $0.77 \leq \tau^*/\tau_c^* \leq 1.57$ ). Each experiment lasted 1200 min. Since pilot runs had established that fluctuations in transport rate decreased markedly over the first 360 min of each experimental run and had fallen to  $\sim 1\%$  of the initial fluctuations after 600–900 min, this ensured that the final surfaces generated in each experiment were produced by a sustained period of quasi-steady transport, [see also Mao *et al.*, 2011]. In all cases, flows were steady and uniform through the test section with a relatively stable water surface.

Sediment collected in a sediment trap at the downstream end of the working section was periodically reintroduced at the upstream end of the flume to provide a form of sediment recirculation appropriate for coarse-grained materials [Wilcock and McArdell, 1993; Mao *et al.*, 2011]. For the first 60 min of each experiment, transport rates were high due to the unconsolidated nature of the bed. Accumulated sediment was therefore reintroduced more frequently during these early stages of the experiments. Reintroductions took place every 10 min for the first half an hour, every 15 min during the following half an hour, and thereafter at  $t = 120, 180, 360, 620,$  and  $900$  min. Pilot runs demonstrated that during the first 120 min of each experiment, the intervals for bed load reintroduction were long relative to rates of bed adjustment. In this case, reintroduced sediment was added to a system which had already adjusted to a lower transport rate than that which moved it into the trap and, instead of maintaining an equilibrium, created a static deposit at the upstream feed area. Reintroducing the full volume of sediment produced in the previous interval was therefore inappropriate. Instead, we used pilot runs to establish the amount of sediment that was anticipated to be produced in each interval. Then at each reintroduction period during the first 120 min the amount of sediment that was reintroduced was equivalent to the yield anticipated for the next sampling period (care was taken to ensure that the grain-size distribution of the reintroduced sediment was representative of the grain-size distribution of the sediment caught in the trap).

### 2.3. Experimental Procedure

For each experiment, the flume was set to the desired slope and the initial surface prepared by running the flume for 30 min at 10 mm flow depth ( $0.003 \leq \tau^* \leq 0.007$ ) in order to remove any artifacts of the screeding

was stopped and the flow was allowed to drain naturally. This was observed to stop transport immediately without causing any obvious disturbance to the bed surface, e.g., by drawing fines down through the bed surface. The test section was not removed from the flume until it had entirely drained so as to further minimize disturbance. The tray was removed using an overhead lifting device that enabled the tray to be lowered onto a bench beside the flume for scanning. Insertion of the tray back into the bed was aided by a retainer of mesh fencing that prevented collapse of the surrounding bed when the tray was removed.

process (e.g., any particularly unstable grains) and to displace any air. The bed was drained, and the test section was removed from the flume. The surface topography was then captured and an area in the center of the test section photographed for the determination of surface grain size. The test section was then replaced, and the flow restarted. This procedure was repeated a further eight times during each experiment producing photographs of the surface grain-size distribution and surveys of the surface topography at 0, 30, 60, 120, 180, 360, 620, 900, and 1200 min. These intervals were chosen on the basis of pilot runs in which the transport rate initially declined very rapidly, suggesting that the greatest change in surface conditions would happen at the beginning of the experiment [e.g., Pender *et al.*, 2001]. Bed load data were collected in association with the sediment recirculation protocol discussed above. That is, prior to recirculation, sediment from the trap was weighed to give estimates of bed load transport rate at  $t = 10, 20, 30, 45, 60, 120, 180, 360, 620, 900,$  and 1200 min. For each experiment, the average value of bed shear stress was calculated as  $\tau = \rho g R S$ , where  $\rho$  is density of water,  $g$  is acceleration due to gravity,  $R$  is hydraulic radius, and  $S$  is slope (corrected for sidewall effects using the method of Williams [1970]). For each surface, values of dimensionless shear stress were calculated as  $\tau^* = \tau / (\rho_s - \rho) g D_{50}$ , where  $\rho_s$  is the density of the sediment (taken to be  $2650 \text{ kg m}^{-3}$ ) and  $D_{50}$  is the median particle size of the bed surface.

Bed surface grain-size distributions were determined from photographs of the removable test section each time it was removed from the flume for scanning. The surface grain-size distribution was sampled by superimposing a grid over the photographs and noting the colors of grains falling under the grid intersections [Wilcock and McArdell, 1993]. Each sample comprised 400 point counts taken from the same  $400 \times 400 \text{ mm}$  area of the test section using a 20 mm square grid.

The topography of the test section was captured using a hand-held laser scanner (Faro Laser Line Probe<sup>®</sup>) mounted on a seven-axis articulated arm (Faro ScanArm<sup>®</sup>). Although the arm provides for the free and easy movement of the laser over and around the complex geometry of the bed, it proved difficult to use within the confines of the flume walls, hence the need for the removable test section. Once the test section had been removed from the flume, the surface was scanned in numerous overlapping short strips up to 60 mm wide with a point density of up to 640 points per scan width and precision of 0.086 mm. The resultant point clouds were aligned and registered to a local coordinate system as a single point cloud using Polyworks<sup>®</sup> proprietary software. Although the resultant point clouds are in 3-D, algorithms that produce fully 3-D surfaces from 3-D point clouds are complex and have significant processing requirements. Following Hodge *et al.* [2009a], therefore, the point clouds were filtered by removing points lying directly beneath, or close to, a high point with the same  $(x, y)$  coordinates using a point spacing of 0.05 mm. In effect, the filter ensures that each  $(x, y)$  location in the point cloud becomes associated with a single elevation ( $z$ ). Digital Elevation Models (DEMs; hereafter referred to as the source DEMs) were then created by interpolating the filtered data onto a 0.15 mm grid using the inverse distance weighting algorithm in ArcGIS<sup>®</sup>. This resolution provides multiple points on any of the smallest grains on the surface, thereby maximizing the chances of including them in the bed topography. The source DEMs were cropped to a rectangular footprint of  $990 \times 390 \text{ mm}$  and then linearly detrended to remove any large-scale slope. These DEMs are subsequently referred to as the measured DEMs.

#### 2.4. Methods of Analysis

Bed surface grain-size distributions and associated percentiles were calculated from the grain-sizes measured using the photographic technique described above. Bed structure was defined using the morphometric measures defined in Table 2, some of which were calculated as a function of scale.

Probability density functions (PDFs) of surface elevations and their properties (i.e., range ( $R$ ), standard deviation ( $s$ ), skewness ( $Sk$ ), and kurtosis ( $Ku^*$ )) were calculated using equations (1)–(4) in Table 2. Although such parameters are relatively crude descriptors of bed microtopography, several workers have shown them to reflect surface-forming processes [e.g., Marion *et al.*, 2003; Aberle and Nikora, 2006; Mao *et al.*, 2011; Mao, 2012]. The area ratio ( $A_r$ ) was calculated using equation (5) to provide a measure of surface roughness [Hobson, 1972; Grohmann *et al.*, 2011; Brasington *et al.*, 2012]. This is a ratio between the actual and plan surface areas [cf. Grohmann, 2004, Figure 10] and is thus large for rough surfaces and close to one for smooth ones. Equation (5) represents a standard method of calculation based on a surface derivative [e.g., Horn, 1981; Grohmann, 2004] and is equivalent to, but simpler to implement than, that of Brasington *et al.* [2012] and Grohmann [2004]. The inclination index ( $I$ ) of Smart *et al.* [2004] was calculated to highlight the



**Table 2.** Metrics Used to Quantify Bed Surface Structure in This Study<sup>a</sup>

Equation	Parameter	Formula
(1)	Range (R)	$z_{95} - z_5$
(2)	Standard deviation (s)	$\frac{1}{n-1} \sum_{i=1}^n (z_i - \bar{z})^2$ ; $\bar{z} = \frac{1}{n} \sum_{i=1}^n z_i$
(3)	Skewness (Sk)	$\frac{1}{n s^3} \sum_{i=1}^n (z_i - \bar{z})^3$
(4)	Kurtosis (Ku*)	$\left[ \frac{1}{n s^4} \sum_{i=1}^n (z_i - \bar{z})^4 \right] - 3$
(5)	Area ratio (A <sub>R</sub> )	$\frac{1}{n} \sum_{i=1}^n \frac{1}{\cos(\theta_i)}$
(6)	Inclination index (I)	$\frac{i^+ + i^-}{i^+ + i^- + i^0}$
(7)	Semivariance ( $\gamma(h_x, h_y)$ )	$\frac{1}{2n-1} \sum_{i=1}^n (z_{i+h} - z_i)^2$

<sup>a</sup> $z_{95}$  and  $z_5$  are the 95th and 5th percentiles of the distribution of bed elevations respectively,  $z_i$  represents the bed elevation at the  $i$ th location,  $n$  is the number of observations,  $\theta_i$  is the magnitude of dip in the direction of steepest descent,  $i^+$  is the number of downstream adjacent point pairs with positive inclinations (where elevation decreases in the flow direction),  $i^-$  is the number of downstream adjacent point pairs with negative inclinations (where bed elevation increases in the flow direction),  $i^0$  is the number of downstream adjacent point pairs with no difference of elevation, and  $\gamma(h_x, h_y)$  is the semivariance estimated from 10,000 randomly, independently located point pairs for each lag  $h$  taken in downstream ( $h_x$ ), cross stream ( $h_y$ ), or in all directions ( $h_x, h_y$ ) as appropriate.  $R, s, Sk, Ku, I$ , and  $(h_x, h_y)$  are calculated for each DEM at full resolution (i.e., elevations on a 0.15 mm grid).  $A_R$  is estimated from DEMs at resolutions of 5 and 60 mm.

development of grain imbrication (equation (6) in Table 2). The index reflects the balance between the number of downstream and upstream facing slopes and is negative for an imbricated bed [see Hodge et al., 2009b, Figure 2].

Variogram analysis [e.g., Oliver and Webster, 1986; Robert, 1988; Butler et al., 2001] was used to provide a further view on topographic variation with scale. In this study, the spatial dependence of the relief across the experimental surfaces was evaluated using directional variograms constructed in the downstream ( $\gamma(h_x, 0)$ ) and cross-stream ( $\gamma(0, h_y)$ ) directions and using 2-D variogram surfaces ( $\gamma(h_x, h_y)$ ), where  $\gamma$  is the semivariance calculated for a number of spatial lag distances ( $h$ ) measured in the downstream ( $h_x$ ) and cross-stream ( $h_y$ ) directions (equation (7) in Table 2) for  $1 \leq h_x \leq 490$  mm and  $1 \leq h_y \leq 190$  mm. The upper limits of  $h_x$  and  $h_y$  approximate half of the downstream and

cross-stream dimensions of the surface, respectively, and ensure that sufficient pairs of points can be sampled from the surface at the longest lags in order to calculate  $\gamma$  accurately [Klinkenberg, 1994]. The lower limit of  $h$  was chosen to minimize the influence of the subgrain-scale microtopography [cf. Butler et al., 2001].

Directional variograms of gravel-bed river roughness often have a characteristic form that can be divided into three regions [Nikora et al., 1998; Nikora and Walsh, 2004; Cooper and Tait, 2009; Mao et al., 2011]. At large spatial lags there is a saturation region where  $(h_x, h_y) \rightarrow s^2$ , and the data exhibit no spatial dependence. At short spatial lags there is a scaling region where the variogram takes the form of a power law  $\gamma = ch^{2H}$ , where  $c$  is a constant and  $H$  is the Hurst scaling exponent. In between these two regions is a curved, transition region. Taken together, the scaling and transition regions define the lag distance termed the range ( $h_r$ ) of the variogram. The spatial lags at the upper ( $h_1$ ) and lower ( $h_2$ ) limits of the scaling and saturation regions, respectively, are important properties of the variogram: the former defines a characteristic, horizontal, bed-roughness scale while the latter defines the correlation length of the bed surface elevations [Cooper and Tait, 2009]. The value of the Hurst exponent ( $H$ ) is also significant because it provides a scale independent measure of positive autocorrelation (or persistence) of bed elevations for  $1 \leq h \leq h_1$  mm [Robert, 1988]. Following Bergeron [1996], objective estimates of these parameters were defined by linear spline interpolation [Smith, 1979] whereby  $h_1$  and  $h_2$  are defined by the two knots of a three degree spline and the scaling exponent  $H$  is defined by the gradient of the line fitted to the scaling region ( $1 \leq h \leq h_1$ ). The model was implemented in log-log space using the PROC NLIN function of the SAS software package [Freund and Littell, 2000]. The slope of the third line segment (fitted to the saturation region;  $h > h_2$ ) was constrained to be zero because the semivariance in this region approximates the sample variance.

### 3. Results

#### 3.1. The Bed Load Dynamic

The character of the bed load dynamic in each of the experiments is shown in Figure 2. The different experiments share the same pattern of variation in that bed load transport rates were initially high, but decreased rapidly during the early stages of each run, with much of the adjustment occurring in the first 120 min

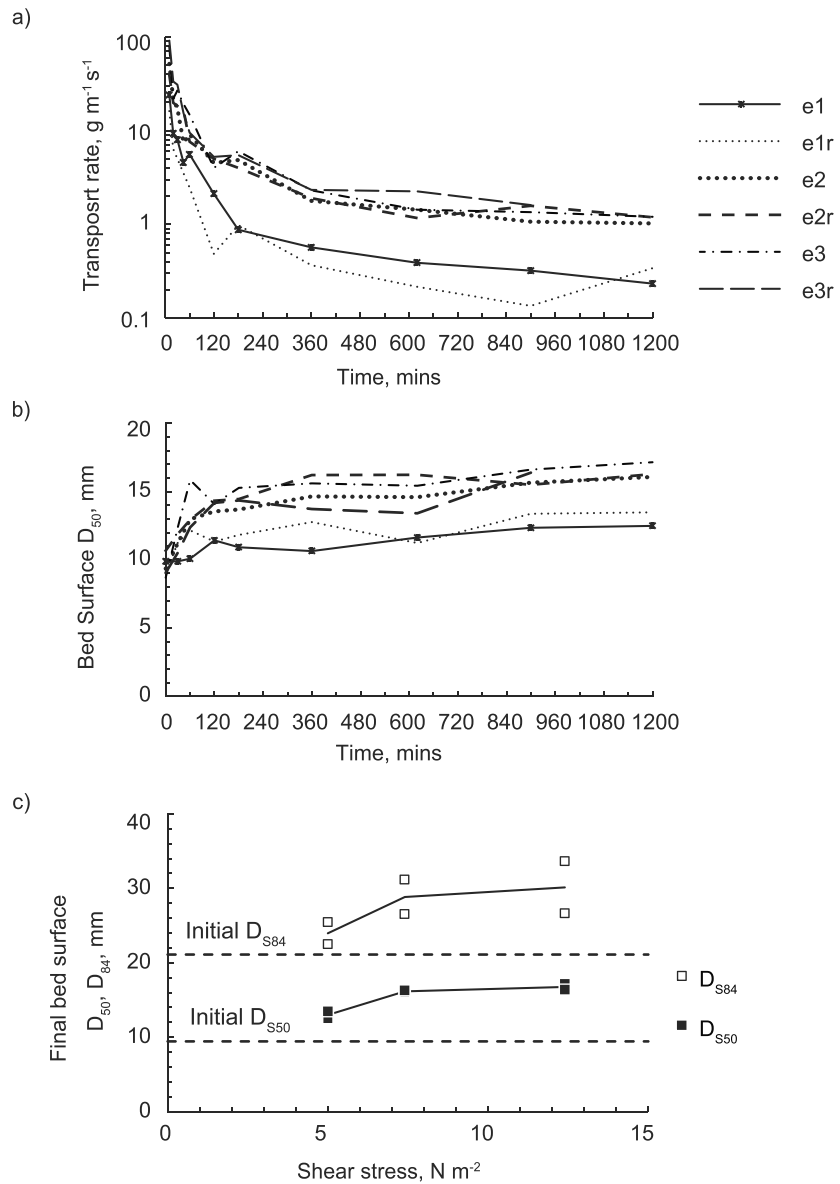


**Figure 2.** (a) Variation in bed load transport rate and (b) median particle size of the bed surface (key as in Figure 2a) with time and (c) variation in median particle size and  $D_{84}$  of the final bed surfaces with shear stress for each experiment and its replicate. In Figures 2a and 2b, the data points are shown for one of the experiments (e1) for reference. In Figure 2c, the dashed horizontal lines represent the average  $D_{50}$  and  $D_{84}$  of the six initial experimental surfaces; the solid lines represent the  $D_{50}$  and  $D_{84}$  of the final surfaces when averaged for each experiment and its replicate.

(Figure 2a). Some further adjustment occurred over the next 240 min as transport rates declined less rapidly; thereafter, transport rates averaged over 260–300 min stabilized (the average difference in transport rate between sampling intervals is  $-0.12 \text{ g m}^{-1} \text{ s}^{-1}$ ), though some experiments (most notably experiment e2) continued to decline indicating that steady state conditions were approximated. The final transport rates varied by a factor of 7 between the three experiments and, as expected, increased with imposed shear stress. The increase in transport rate between experiments e2, e2r and e3, e3r (where  $\tau^* \approx 0.028$  and  $0.046$ , respectively) was not, however, as great as that between experiments e1, e1r and e2, e2r (where  $\tau^* \approx 0.023$  and  $0.028$ , respectively). The reduced sensitivity of transport rate at the higher flow strength is unexpected and may reflect either a reduction in transport stage ( $\tau^*/\tau_c^*$ ) as a result of a structure-induced increase in entrainment thresholds and/or a roughness-induced reduction in the available shear stress or a limitation of sediment supply as a consequence of the manner by which sediment was recirculated. The latter, however, seems more likely given that our

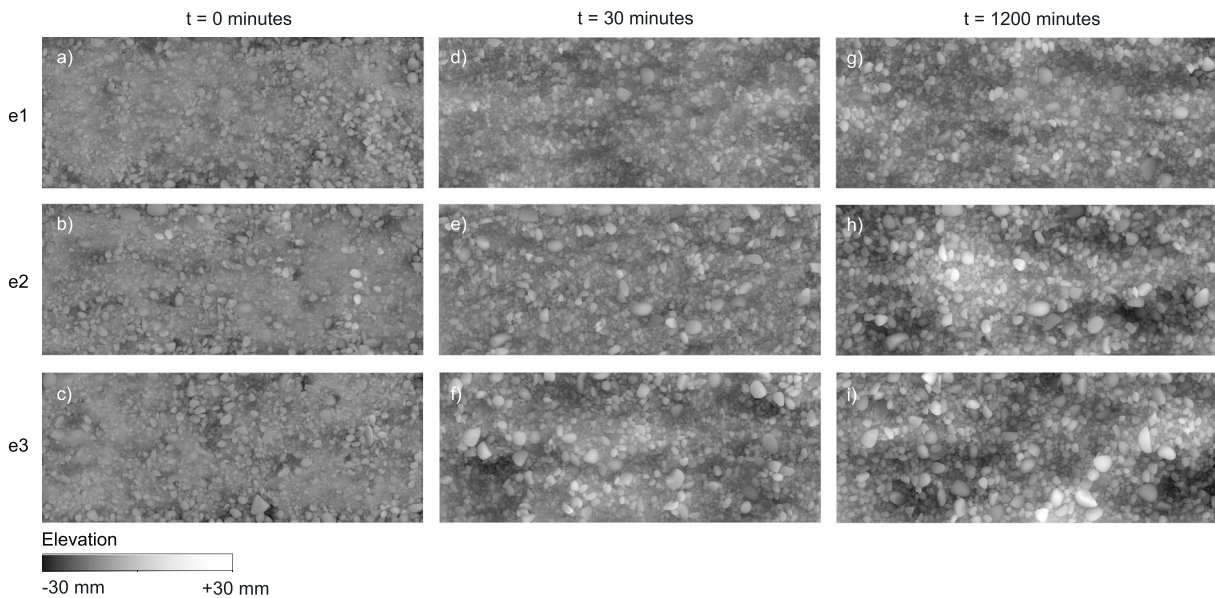


**Figure 3.** Digital elevation models of bed surface topography for experiments e1, e2, and e3 at (a–c)  $t = 0$ , (d–f) 30, and (g–i) 1200 min. The bed area is  $990 \times 390$  mm, and the flow direction is from left to right.

analyses of the bed surface condition described below indicate little difference in the surface structure and roughness of the beds developed in experiments e2 and e3. Changes in the bed surface grain-size are shown in Figure 2b. During the experiments, the bed surface developed a coarse surface armor layer as the proportion of fine and coarse grains in the surface size distribution decreased and increased, respectively. As with the transport rates, most of the adjustment in surface grain size occurred in the first 120 min and had largely been completed by  $t = 360$  min. Figure 2c compares the  $D_{s50}$  and  $D_{s84}$  of the final armored beds. It suggests that the armor layers coarsened from e1 to e2 but that little further coarsening was observed at the higher shear stress applied in e3. Inspection of the bed load grain-size distributions suggests that there was little preferential winnowing of fines from the surface which, under the sediment recirculation protocol, might have promoted the coarsening of the surface. Instead, surface coarsening is attributed to a gravity-driven kinematic sorting process in which finer grains preferentially move into voids left behind by entrained grains [Parker and Klingeman, 1982]. Since the kinematic sorting process is not thought to depend explicitly on the rate of transport, mobile armors that are invariant with flow strength are the expected pattern of equilibrium bed surface adjustment in a laboratory flume when the sediment output is recirculated [Wilcock and McArdeell, 1993; Wilcock, 2001; Mao et al., 2011].

### 3.2. Visualization of the DEMs

Some examples of the measured DEMs of the experimental surfaces are shown in Figure 3. The screeded beds (Figures 3a–3c) had a flat uniform surface with random grain-scale variations in bed elevation about the mean. The impression was of a loose arrangement of particles. In contrast, the water-worked surfaces comprised well-packed, imbricated particles and displayed considerable heterogeneity at the mesoscale (10–100 mm) with patches of lower and higher bed elevations clearly discernible (Figures 3d–3i). The water-worked topography developed rapidly with the onset of sediment transport (it was clearly evident in the surfaces at  $t = 30$  min (Figures 3d–3f)) and the mesoscale topography was more pronounced in experiments e2 and e3 which were run at higher shear stresses (Figures 3g–3i). The spatial structure of the mesoscale topography varied over the duration of each experiment and was reminiscent of the longitudinal ridges and troughs which appear to characterize many water-worked beds [Marion et al., 2003; Hodge et al., 2009b; Cooper and Tait, 2009; Bertin and Freidrich, 2014] and may reflect the development of secondary flow cells [McLelland, 2013]. At the grain scale, clusters of particles were observed in the water-worked beds, but they did not appear to be a significant feature of the bed topography. This may reflect the narrow grading of the experimental mixture.



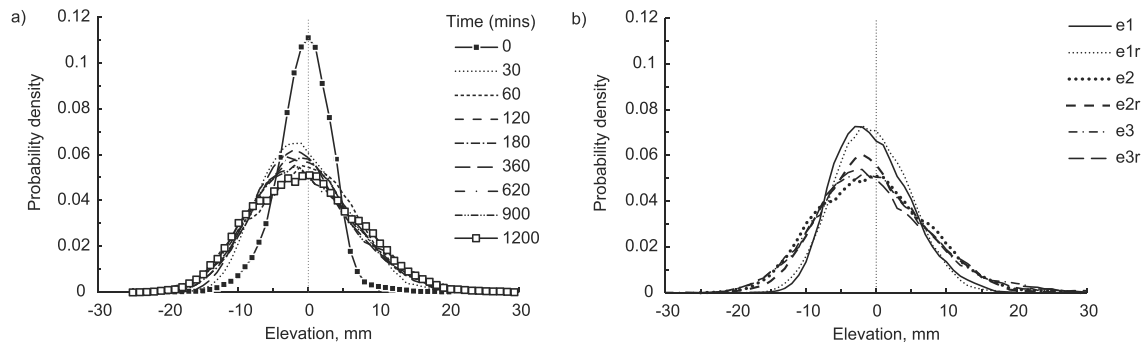


**Figure 4.** Probability density functions of bed surface elevations for (a) all the surfaces of experiment e2 and (b) the final surface of each experiment. In Figure 4a, the data points are shown for  $t = 0$  and 1200 min for reference and to highlight the initial and final surfaces.

### 3.3. Probability Density Functions of Bed Elevations and Their Moments

During each experiment, the range and standard deviation of bed elevations increased, the number of observations around zero mean decreased, and the PDFs become positively skewed with broader, flatter peaks. The dynamic of this adjustment is illustrated in Figure 4a which shows the temporal evolution of bed elevation PDFs in experiment e2. The initial, screeded bed was characterized by a narrow, peaked distribution with slight negative skew and positive kurtosis. These characteristics were shared by all of the start-up beds and indicate consistency in the preparation of the initial surfaces. The most significant adjustment in the shape of the PDFs occurred in the first 30 min as the range and standard deviation increased by 7.4 mm and 2.2 mm, respectively, and the maximum probability density decreased from 0.11 at zero mean elevation to 0.06 at an elevation of  $-2$  mm. Thereafter, changes in the shape of the PDFs are relatively modest. This pattern of adjustment was observed in all experiments, though the magnitude of the adjustment varied between treatments. A comparison of the PDFs for the final surface of each experiment indicates that higher flows generated broader, flatter distributions with heavier tails (Figure 4b).

Further insight into the nature of the bed surface adjustment under different flow strengths can be obtained by considering the evolution of the statistical moments of the bed elevation distributions. These are generally consistent between replicates of each experiment. For each experiment, Figure 5 shows how standard deviation, skewness, and kurtosis varied over time (Figures 5a–5c) and how the moments calculated for the final, equilibrium surfaces varied with dimensionless shear stress (Figures 5d–5f). Much of the adjustment in standard deviation occurred in the first 120 min of each experiment with little change occurring thereafter (Figure 5a). The standard deviation of the equilibrium surfaces increased from 5.4 mm at the lowest flow to 7.1–7.7 mm at the intermediate flow, with only a modest further increase at the highest flows ( $s \approx 8$  mm; Figure 5d). Figure 5b shows that, with one exception (e2r), the bed elevation PDFs shifted from negative to positive skew within the first 30 min of each experiment, with surfaces exhibiting either near-symmetrical ( $Sk \approx 0$ ) or positively skewed PDFs thereafter. Kurtosis also adjusts rapidly during the early stages in the experiments, reflecting a shift to more platykurtic distributions (Figure 5c), although the variation thereafter is more pronounced than that seen in either  $s$  or  $Sk$ . Comparison of values of  $Sk$  and  $Ku^*$  for the final surfaces in each experiment suggests that higher flows generate beds with greater positive skew and kurtosis (Figures 5e ( $r = 0.73$ , and  $p = 0.097$ ) and 4f ( $r = 0.96$ , and  $p < 0.05$ ), where  $r$  is the Pearson Product Moment correlation coefficient).

### 3.4. Variograms

The downstream  $\gamma(h_x, 0)$  and cross-stream  $\gamma(0, h_y)$  variograms for both screeded and water-worked beds approximate the model described above: that is, each variogram can be subdivided into scaling, transition and saturation regions at short, intermediate, and long lags, respectively. By way of illustration, Figure 6 shows the downstream variograms for all the surfaces measured in experiment e2 and for the final surfaces in each experiment.

In general, the spline model provided a good fit to the data and generated coherent and consistent estimates of  $h_1$  and  $H$ . Considering all experiments, the goodness of fit statistic  $r^2$  for the downstream variograms, for

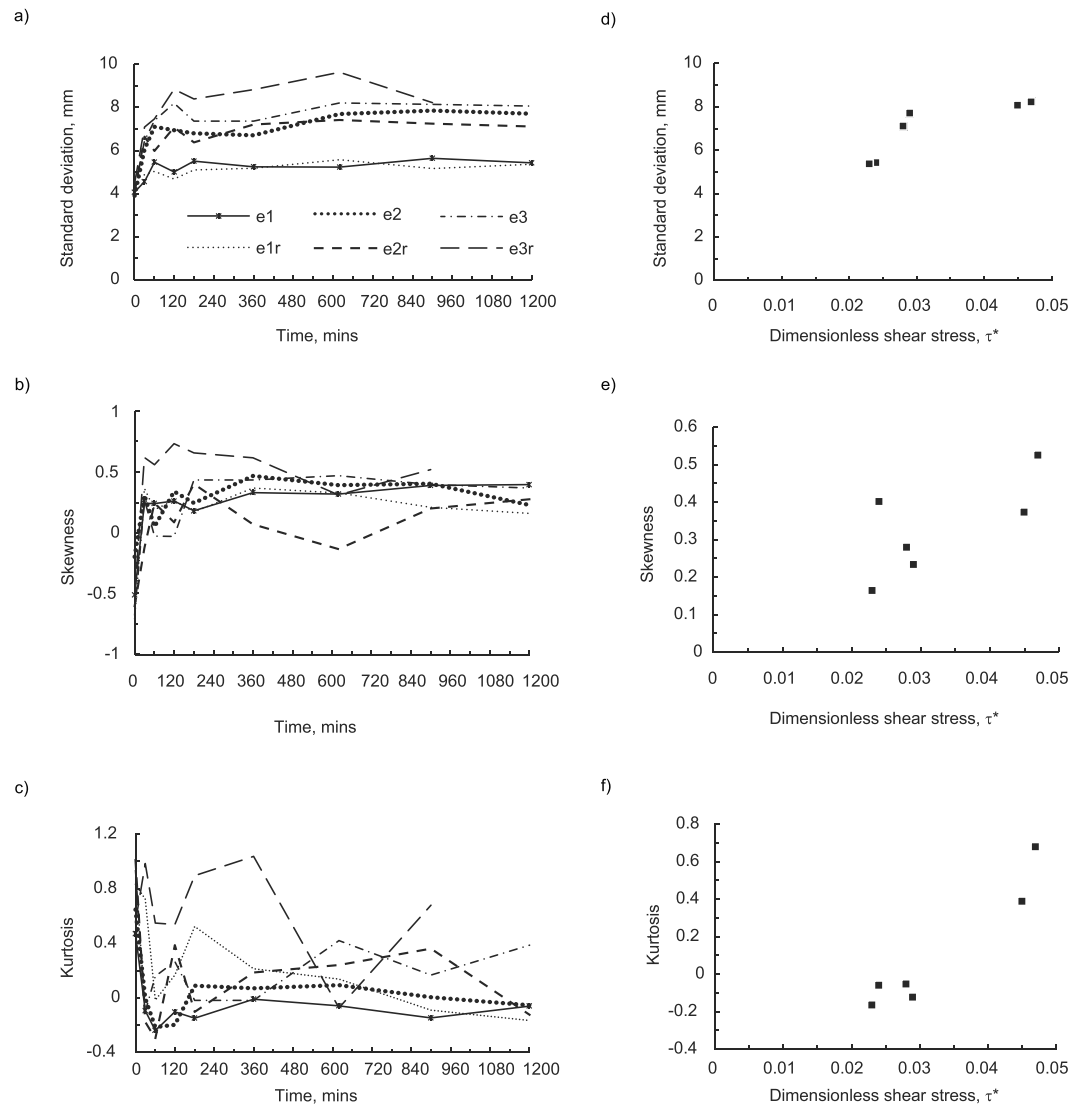


**Figure 5.** Variation in standard deviation, skewness, and kurtosis of the bed elevation PDFs for (a–c; key as in Figure 5a) all the surfaces in each experiment with time and for (d–f) the final surface of each experiment with flow strength. In Figures 5a–5c, the data points are shown for one of the experiments (e1) for reference.

example, varies between 0.991 and 0.999 and the 95% confidence limits associated with the estimates of  $h_{1x}$  and  $H_x$  are of the order 1–2 mm and 6–8%, respectively. Notwithstanding the high  $r^2$  values, plots of the residuals for  $h_x \leq h_{1x}$  reveal a convex upward shape, highlighting the presence of nonlinearity in this region of the variogram. This suggests that a scale-independent scaling region does not perfectly describe the surfaces at short lags and that the parameters  $h_1$  and  $H$  need to be interpreted cautiously. Caution also needs to be exercised in respect to the estimates of  $h_2$  since these are highly variable, subject to large errors and difficult to reconcile with the expected roughness characteristics of the surfaces. It might be expected, for example, that the transition region for the screeded beds would be relatively narrow so that  $h_2 \approx h_1$ . This is because these surfaces should not have exhibited any substantive variations in bed topography larger than the grain scale. However, with the exception of experiment e1 ( $h_{2x} = 37 \pm 6$  mm), estimates of  $h_{2x}$  are many times greater than  $h_{1x}$  and larger, even, than the maximum particle size ( $72 \leq h_{2x} \leq 342$  mm), with 95% confidence intervals of several tens of millimeters (Figure 6a). These high values probably reflect the difficulty in screeding a gravel bed completely flat and illustrate the sensitivity of  $h_2$  to small variations of the medium-scale topography. In many cases, the sills are also poorly defined, suggesting that the sampling area may be too small. Values of  $h_2$  for the water-worked surfaces are generally higher, reflecting the development

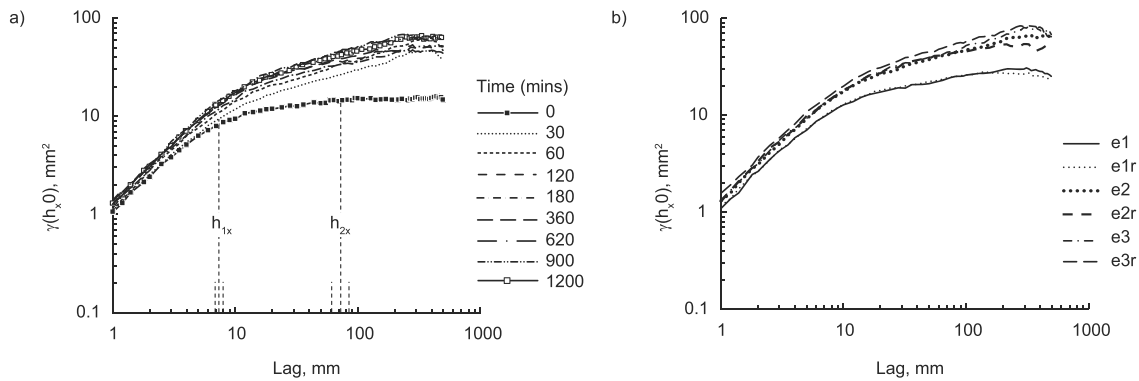


**Figure 6.** Downstream variograms for (a) all the surfaces measured in experiment e2 and (b) the final surfaces in each experiment. In Figure 6a, the dashed lines indicate estimates of  $h_{1x}$  and  $h_{2x}$  and their 95% confidence intervals for the screeded surface. Figure 6a also shows the data points for  $t = 0$  and 1200 min for reference and to highlight the initial and final surfaces.

of the mesoscale topography during the experiments (Figure 3). The number of mesoscale forms contained within the test section was, however, low, and estimates of  $h_2$ , therefore, are highly variable. In the light of these difficulties in generating meaningful and generalizable estimates of  $h_2$ , they are not considered further.

As expected, the topography of the screeded surfaces was isotropic with a roughness structure and scaling that was consistent with the random arrangement of individual grains ( $h_{1x} \approx h_{1y} \approx D_{s50}$ ;  $H_x \approx H_y \approx 0.5$ ). Interestingly, many values of  $H$  are slightly in excess of 0.5. This reflects a deviation from a truly random topographic structure and is thought to reflect the presence of some larger surface grains, due to their greater radii, means that sequences of heights across their tops exhibit positive autocorrelation. Over time, sediment transport forced a series of bed adjustments characterized by increases in bed roughness ( $(h_x, 0)$ ), the scaling region ( $h_{1x}$ ) and the scaling exponent ( $H_x$ ), as illustrated by the evolution in variogram form (Figure 6a) and by the corresponding temporal variation in  $h_{1x}$  and  $H_x$  (Figures 7a and 7b). Estimates of  $(h_y, 0)$ ,  $h_{1y}$ , and  $H_y$  also increased during each run. For all water-worked surfaces ( $n = 47$ ), little difference is observed between the downstream and cross-stream estimates of either  $h_1$  ( $\bar{h}_{1x} = 10.1$  mm,  $\bar{h}_{1y} = 10$  mm, and  $\bar{h}_{1x}/\bar{h}_{1y} = 1.02$ ) or  $H$  ( $\bar{H}_x = 0.56$  mm,  $\bar{H}_y = 0.58$  mm, and  $\bar{H}_x/\bar{H}_y = 0.97$ ). The water-worked surfaces are, therefore, isotropic in  $h_1$  as well as  $H$ . A comparison of the variograms for the final surfaces of each experiment does, however, suggest a dependency of surface structure on flow strength (Figure 6b). This dependency is quantified in Figures 7c and 7d which shows that the scaling region ( $h_1$ ) and exponent ( $H$ ) in both downstream and cross-stream directions increased from e1 ( $\tau^* \approx 0.024$ ) to e2 ( $\tau^* \approx 0.029$ ), with no further increase at the highest flow strength in e3 ( $\tau^* \approx 0.046$ ).

The evolution of bed surface character is also evident in the 2-D variograms. As an example, Figure 8 shows the 2-D variograms for the surfaces of experiment e2 at  $t = 0, 30,$  and 1200 min and the variation in the ratio of the downstream and cross-stream semivariance ( $(h_x, 0)/(0, h_y)$ ). The isotropic nature of the initial surface is confirmed by the near-circular contours in Figure 8a which indicates that the change in  $\gamma$  with lag distance was similar in all directions. As shown in Figure 8d, the ratios  $\gamma(h_x, 0)/\gamma(0, h_y)$  for the initial surface closely approximate unity: the range of correlated data for all initial surfaces of all the experiments (approximately  $1 \leq h \leq 50$  mm;  $n = 155$ ) is  $0.88 \leq \gamma(h_x, 0)/\gamma(0, h_y) \leq 1.14$  with  $0.95 \leq \gamma(h_x, 0)/\gamma(0, h_y) \leq 1.05$  accounting for 70% of all values. The 2-D variograms for the water-worked beds (Figures 8b and 8c) also exhibit circular contour patterns indicative of surface isotropy, but only for short lags (approximately  $h \leq 4$  mm for which  $0.88 \leq \gamma(h_x, 0)/\gamma(0, h_y) \leq 1.10$  in experiment e2; Figure 8d). At longer lags, the contours are elliptical (Figures 8b–8d), reflecting the development of surface anisotropy [Nikora et al., 1998; Nikora and Walsh, 2004; Mao et al., 2011]. The principal axes of the ellipses are generally aligned in the flow direction (increasing  $h_x$ ), indicating the development of a flow-aligned structure.

Particles  $< 4$  mm comprise, on average,  $< 7\%$  of the water-worked, surface grain-size distributions. The scale of the surface isotropy identified in Figures 8b and 8c ( $1 \leq h \leq 4$  mm) approximates, therefore, the smallest grain-size fraction (4–5.6 mm) that makes up a significant proportion ( $\approx 8\%$ ) of the bed surfaces. Since the

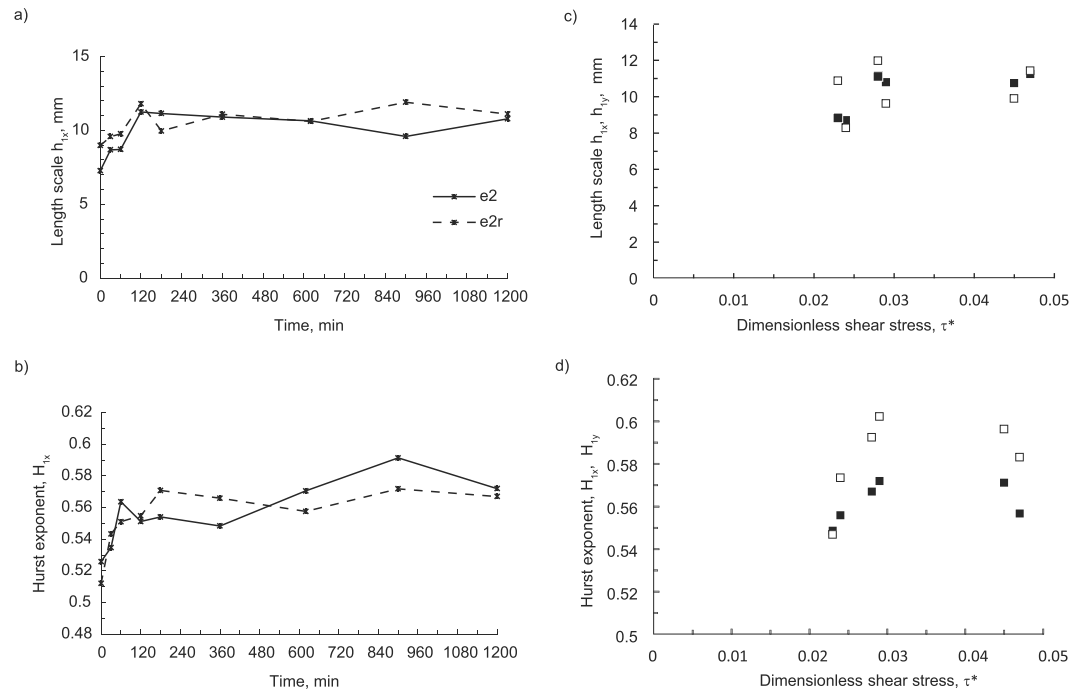


**Figure 7.** Variation in length scales  $h_1$  and Hurst exponents  $H$  for (a, b; key as in Figure 7a) all the surfaces of experiment e2 and its replicate e2r with time (downstream direction only) and for (c, d) the final surface of each experiment with flow strength (downstream (solid symbols) and cross-stream (open symbols) directions). It should be noted that although Figure 7d implies  $H_y > H_x$ , the differences for e1, e1r, and e3r are not statistically significant ( $p > 0.05$ ).

point pairs used to calculate  $\gamma$  at this scale are likely to be on the same grain, the small-scale surface isotropy of the water-worked beds can be attributed to the surface roughness of individual particles [see also Hodge *et al.*, 2009b]. At slightly longer lags ( $4 \leq h \leq 45$  mm), the ellipsoid contours are thought to reflect the preferential orientation of grains with the long axis of the ellipse indicating the alignment of the  $a$  axes [Nikora *et al.*, 1998; Nikora and Walsh, 2004; Hodge *et al.*, 2009b]. In this study, surface anisotropy extends beyond the grain scale which suggests that the flow-aligned structure is some combination of the prevalent alignment of individual particles, clusters of grains and the mesoscale topography described above (Figure 3). Figure 8 confirms that the mesoscale structure developed relatively quickly with the onset of sediment transport and was maintained thereafter for the duration of each run with relatively little modification, despite the changing spatial organization of the component forms (the patches of higher and lower bed elevations).

### 3.5. Area Ratio

As highlighted by Brasington *et al.* [2012],  $A_R$  statistics are highly sensitive to DEM resolution, with increasing grid size associated with lower  $A_R$  values and reduced topographic complexity. In this study, we examine the nature of the adjustment of surface complexity at DEM resolutions of 60 and 5 mm (Figure 9). These scales were chosen on the basis that the results characterize the surface at scales of 180 and 15 mm, respectively, which might, in turn, be expected to correspond with the mesoscale and grain-scale components of the surface topography (100–200 mm (Figure 3) and 13–17 mm (Table 1), respectively). As anticipated, a comparison of Figures 9a and 9b indicates that the coarser scale surfaces were characterized by less surface complexity (lower  $A_r$  values).

At the coarser scale (Figure 9a), the experimental surfaces were initially flat ( $A_R \approx 0$  at  $t = 0$  min) but developed a more complex topography ( $A_R > 0$ ) relatively quickly with the onset of sediment transport. At this scale, the increased complexity of the water-worked beds is consistent with the development of the flow-aligned topography during the experiments as seen in the DEMs (compare, for example, Figures 3b, 3e, and 3h). Interestingly, Figure 9a suggests that e2 and e3 developed more complex surfaces than e1, a difference which is also evident in the DEMs (compare Figures 3g–3i). Similar patterns of adjustment in surface

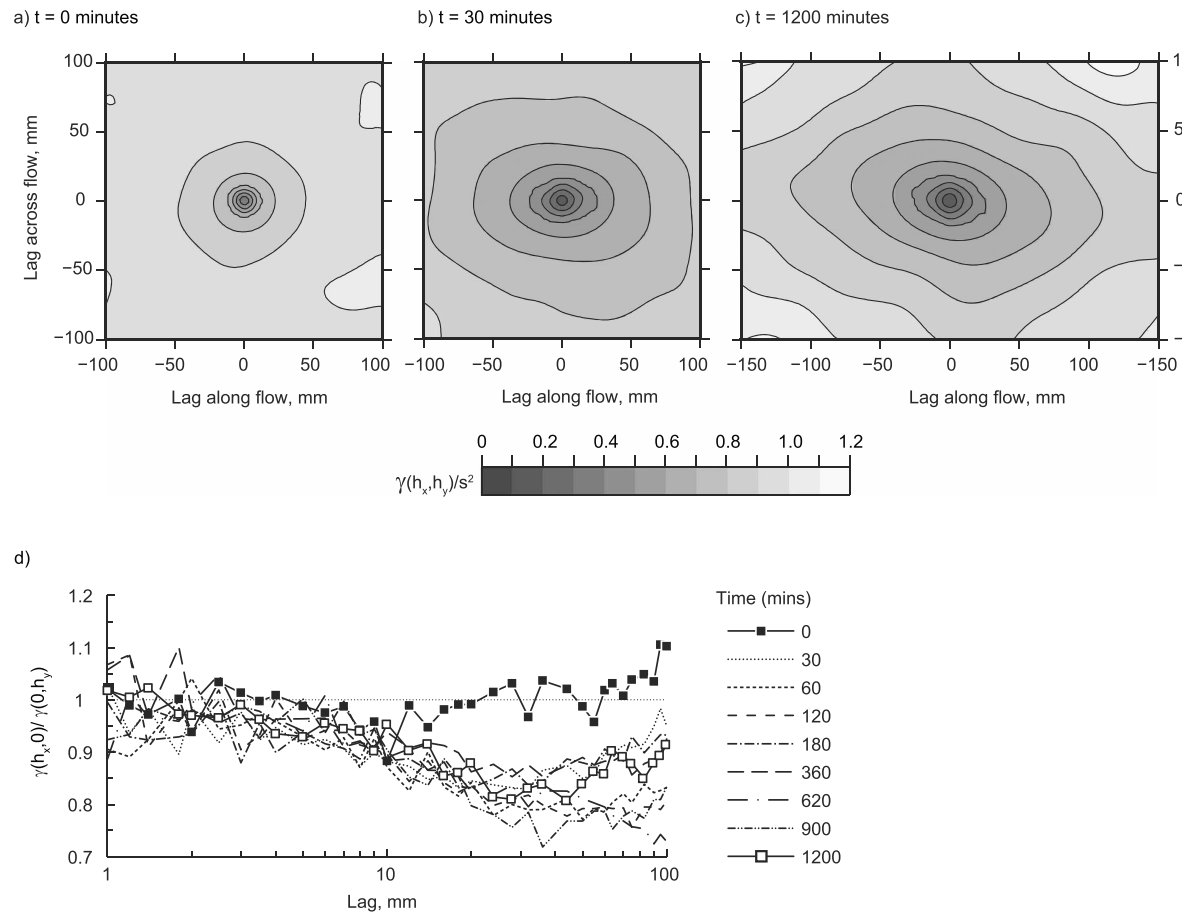


**Figure 8.** Two-dimensional variograms for the surfaces of experiment e2 at (a)  $t = 0$ , (b) 30, and (c) 1200 min. (d) Variation in the ratio  $\gamma(h_x, 0)/\gamma(0, h_y)$  with lag for all time intervals in experiment e2 ( $1 \leq h \leq 100$  mm). Note that the variogram surfaces Figures 8a–8c show the normalized semivariance  $\gamma(h_x, h_y)/s^2$  for  $1 \leq h_{x,y} \leq 100$  mm (Figures 8a and 8b) and  $1 \leq h_x \leq 150$  mm,  $1 \leq h_y \leq 100$  mm (Figure 8c).

complexity were observed at the smaller scale (Figure 9b), and their resemblance to the patterns of grain-size adjustment shown in Figure 2b suggests that they reflect surface coarsening and the development of a mobile armor.

### 3.6. Inclination

Values of  $I$  for the initial and final surfaces of each experiment are compared in Figure 10a. Calculated at the resolution of the DEMs (0.15 mm),  $I$  could have been dominated by grain-surface roughness. However, for the relatively smooth gravels of the experimental mixture, grey-scale plots with  $i^+$  as black and  $i^-$  as white clearly show grain-scale patterns, which demonstrate that the index does reflect particle imbrication ( $i^+$  and  $i^-$  defined in Table 2).

Values for the initial surfaces approximate zero ( $-0.04 \leq I \leq 0.04$ ) indicating that the number of positive and negative inclinations was approximately equal, which is the expected result for screeded beds in which particles show no preferential orientation. Interestingly, however, the index is slightly negative for five of the six screeded beds, which indicates a slight bias toward particles with an upstream inclination and may reflect the fact that the beds were screeded in the direction of flow. In contrast, the inclination indices for the water-worked surfaces vary between  $-0.14$  and  $-0.09$  indicating a predominance of upstream facing slopes and the presence of grain imbrication. The degree of grain imbrication shown by the final surfaces is not sensitive to flow strength (Figure 10a) and is shown to have developed very quickly with the onset of sediment transport (Figure 10b).



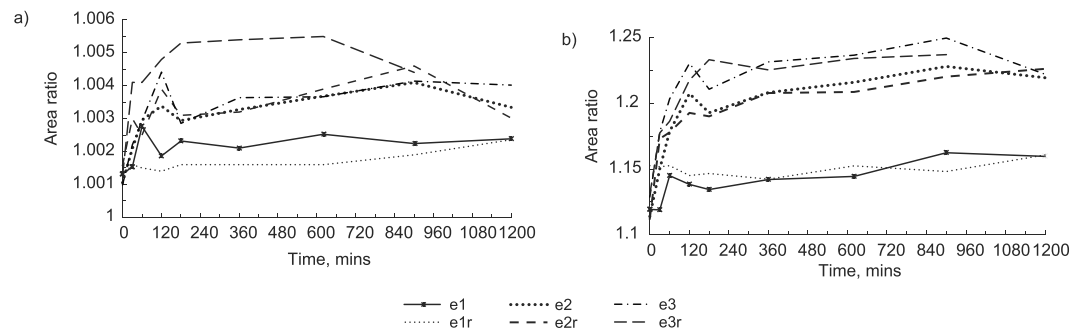


**Figure 9.** Variation in  $A_R$  with time for each experiment as measured at DEM resolutions of (a) 60 mm and (b) 5 mm. Since the calculation of  $A_R$  is undertaken using a  $3 \times 3$  moving window, the surface characterization is at scales of 180 and 15 mm, respectively. Data points are shown for one of the experiments (e1) for reference.

### 3.7. Isolating the Grain and Mesoscale Adjustments of Bed Surface Topography

It is apparent from the results above that the topographic adjustment of the experimental surfaces occurred at two scales: the grain scale (due to surface coarsening and particle alignment) and at the mesoscale (due to the development of patches of higher and lower bed elevations). To clearly more view, and differentiate between, these two components of bed topography, the technique of regional-residual separation (RRS) [Wessel, 1998; Hillier and Smith, 2008] was used to generate surfaces representative of the mesoscale and grain-scale topographies. For each sample period, surfaces representative of the mesoscale were derived by smoothing the source DEMs with a 100 mm boxcar filter and, from this, subtracting the planar trend fitted to the source DEMs. Surfaces representative of the grain scale were then derived by subtracting the output of the boxcar filter from the source DEMs. The filter width of 100 mm approximates  $3D_{s84}$  and approaches the smallest scale where the following aspirational criteria were visually verified: (i) the complete absence of grain-scale topography in the surfaces smoothed with the boxcar filter and (ii) the removal of much of the mesoscale topography in the surfaces representing the grain-scale component. That is, in defining the surfaces representative of the grain scale, we endeavored to filter out as much of the mesoscale topography as possible, while making sure to keep all of the grain-scale topography. Figures 11a and 11b shows the meso and grain-scale topographies of the surfaces generated in experiment e2 at  $t = 0, 30,$  and 1200 min. A comparison with Figure 3 indicates that the RSS technique was largely successful in isolating the two topographic scales with the development of the flow-aligned topography clearly evident in the mesoscale surfaces (Figure 11a; a comparison of Figure 3h with the bottom panel of Figure 11a is particularly instructive in this regard).

Figures 11d and 11e shows the bed elevation PDFs of all the mesoscale and grain-scale surfaces for experiment e2 (note that metrics derived from the mesoscale and grain-scale surfaces are hereafter defined by subscripts  $m$  and  $g$ , respectively). The bed elevation PDFs of the mesoscale bed topography are essentially symmetrical (Figure 11d). Although the form of the PDFs varies somewhat erratically as a function of time, this is to be expected since there were relatively few mesoscale forms in the test section. A Wilcoxon test on  $Sk_m$  values for each experiment indicates, with the exception of e2r, that there is insufficient evidence to reject the null hypothesis that  $Sk_m = 0$  at the 95% significance level. This suggests that the difference in

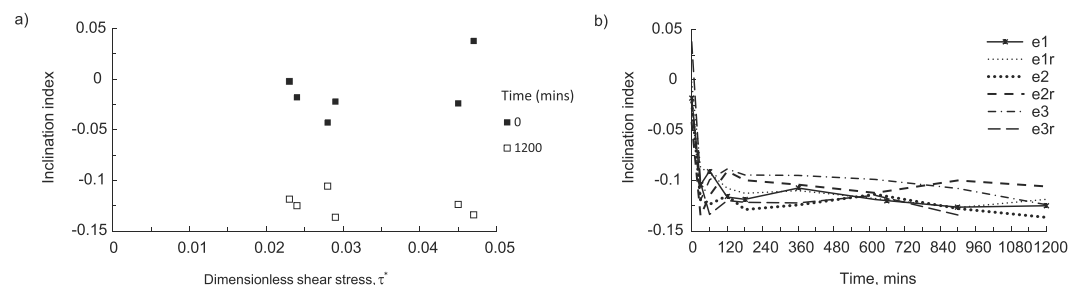


**Figure 10.** Variation in  $I$  for (a) the initial and final surfaces in each experiment with flow strength and for (b) all the surfaces in each experiment with time. In Figure 10b, data points are shown for one of the experiments (e1) for reference.

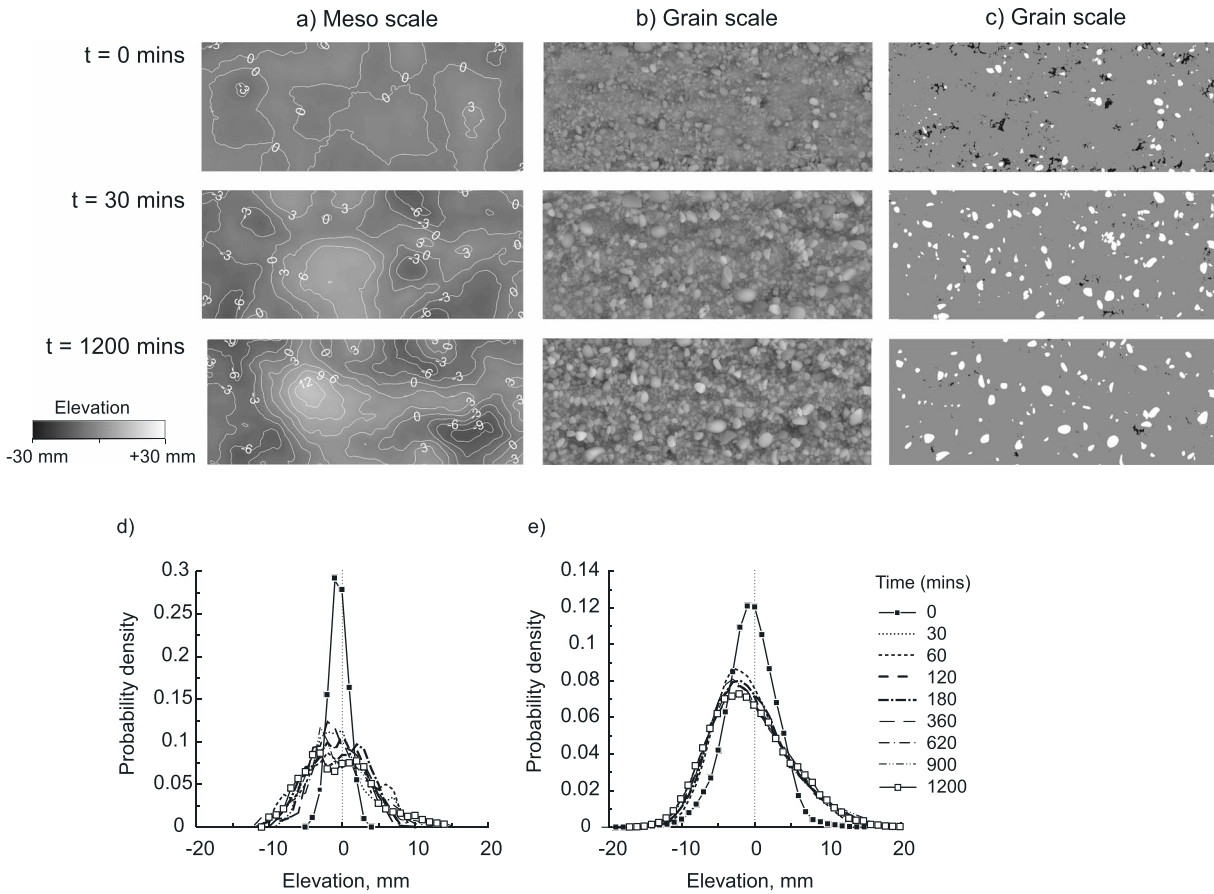


**Figure 11.** Digital elevation models of (a) mesoscale and (b and c) grain-scale surface topography for experiment e2 at  $t = 0, 30,$  and  $1200$  min. Probability density functions of bed elevations for (d) the mesoscale topography and (e) the grain-scale topography for all the surfaces of experiment e2. In Figures 11d and 11e, the data points are shown for  $t = 0$  and  $1200$  min for reference and to highlight the initial and final surfaces. In Figure 11c, elevations more than two median absolute deviations (MAD) above and below the modal ( $M_o$ ) elevation are colored white and black, respectively; all intervening elevations are colored grey. The spatial pattern of elevations greater than  $M_o + 2MAD$  suggests that the extension and fattening of the right-hand tail of the grain-scale bed elevation PDFs (Figure 11e) can be attributed to the increased protrusion of coarser grains above the average bed level.

surface skewness between the screeded and water-worked beds noted above (Figure 5b) is a function of topographic adjustments at the grain scale rather than at the mesoscale. This is confirmed in Figure 11e, which shows that for experiment e2, the grain-scale topography of the screeded surface has negative skew ( $Sk_g = -0.17$ ), while all water-worked surfaces exhibit positive skew ( $0.4 \leq Sk_g \leq 0.57$ ). These contrasts in grain-scale skewness are mirrored across the series of experiments for which  $-0.43 \leq Sk_g \leq -0.17$  and  $0.36 \leq Sk_g \leq 0.74$  for the screeded and water-worked beds, respectively.

Although the utility of isolating different scales of topography is most apparent when considering lumped metrics of bed surface topography such as bed elevation PDFs, it can also help clarify scale-based analyses such as variograms and area ratio statistics (Figures 6–9). For example, the downstream and 2-D variograms for the grain-scale surfaces of experiment e2 (Figure 11b) are shown in Figures 12a and 12c (for comparison, the variograms for the mesoscale surfaces (Figure 11a) are shown in Figures 12b and 12d). As expected, the variograms for the grain-scale surfaces exhibit narrower transition regions, much reduced ranges, and lower sills in comparison to those constructed for the measured surfaces (cf. Figures 6a, 8a–8c, 12a, and 12c). Since  $\gamma_g \approx \gamma$  for  $h < h_{rg}$ , no attempt was made to define estimates of  $h_{1g}$  and  $H_g$ . Grain-scale adjustments both within and between experiments, however, are evidenced in the dependency between estimates of the grain-scale variogram range ( $h_{rg}$ ) and surface grain size. For example, the increase in  $h_{rg}$  for e2 (from about 15 mm for the initial screeded surface to about 30 mm for the water-worked surfaces; Figure 12a) closely matches the increase in surface grain size (from  $D_{s84} = 20$  mm at  $t = 0$  min to  $D_{s84} \approx 33$  mm thereafter; Table 1).

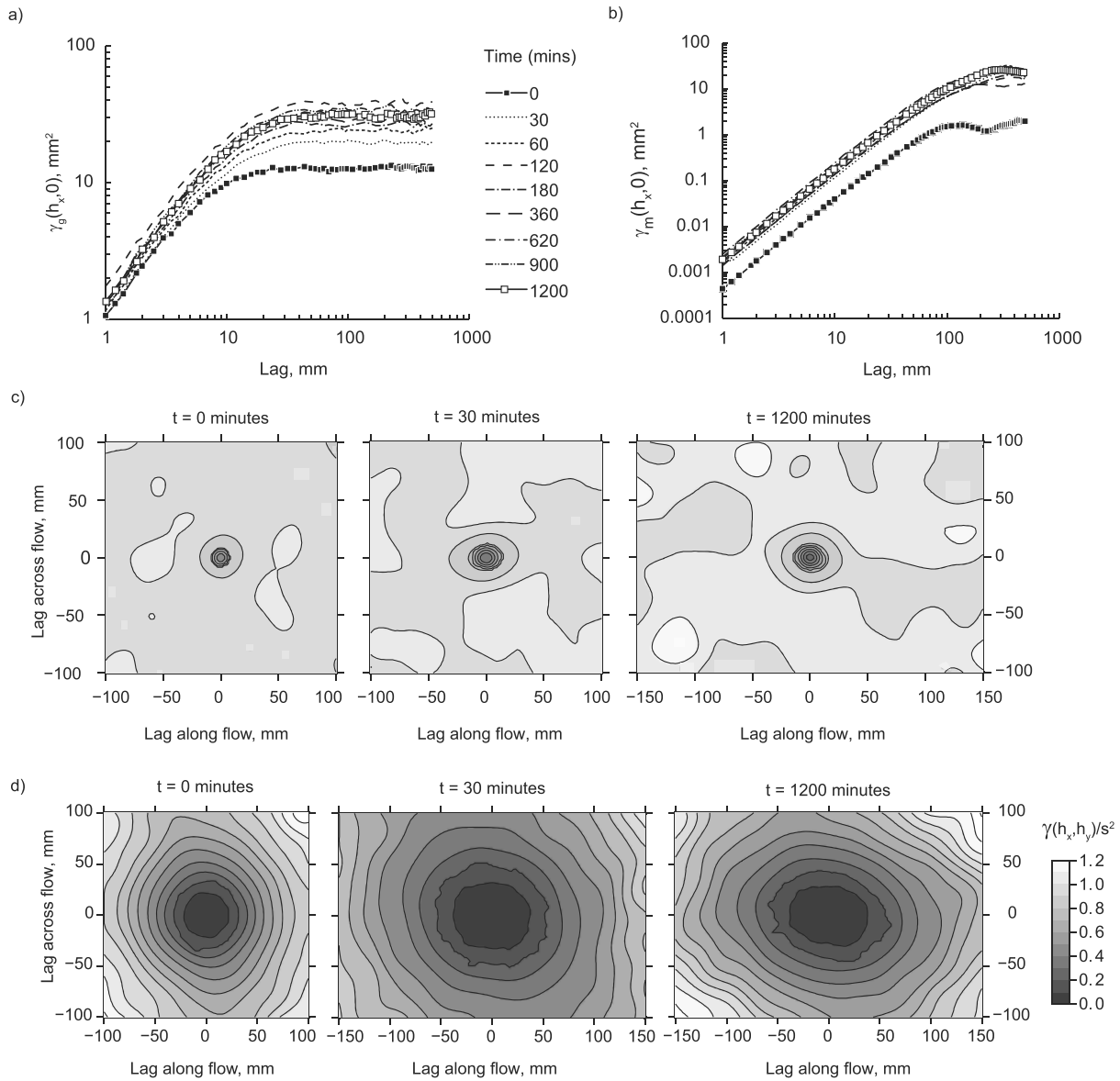


**Figure 12.** Directional downstream variograms for the (a) grain-scale and (b) mesoscale surfaces and 2-D variograms for the (c) grain-scale and (d) mesoscale surfaces of experiment e2. In Figures 12a and 12b, the data points for  $t=0$  and 1200 min are shown for reference and to highlight the initial and final surfaces.

Moreover, the fact that values of  $h_{rg}$  fall within the range of the particle sizes making up the beds supports the observation made above in relation to Figure 3 that small-scale bed forms such as clusters were not a significant feature of the water-worked surfaces [cf. Robert, 1988, 1991; Bergeron, 1996]. It is important, however, to note two important caveats with regard to these observations. The first is that the increase in the range of the grain-scale variograms over the duration of the experiment might, in part, reflect the topographic development of the bed at scales greater than the grain scale because, as discussed above, the RRS procedure was not able to remove all mesoscale features from the grain-scale surfaces. The second is that the shape of the variogram in the transition region and, therefore, the definition of the variogram range will be influenced by spectral overlap between the different scales [Wessel, 1998].

At the mesoscale, the overall variance of the bed elevations for the initial surfaces of each experiment is low ( $s^2 \approx 1-3 \text{ mm}^2$ ; Figure 12b). This is the expected result for a screeded bed. Over time, the range and sill of mesoscale variograms increases, reflecting the development of the larger-scale flow-aligned topography (Figures 12b and 12d). Approximations of the variogram ranges for the final surfaces in each experiment

define downstream and cross-stream length scales for the mesoscale topography as  $\sim 200$  mm and 100 mm, respectively, though these estimates may be constrained somewhat by the size of the test section.

## 4. Discussion

### 4.1. Characteristics of Water-Worked Gravel Beds

Comparison of the initial and final surfaces in each experiment demonstrates anticipated differences between the characteristics of screeded and water-worked gravel beds. As expected, the final beds were armored ( $1.5 \leq D_{s50}/D_{b50} \leq 2.1$ ). Mobile armoring proceeds by the gravity-driven process of kinematic sorting during transport in which finer fractions of the surface bed material work their way into the subsurface through the interstices of the bed and via the pockets left by entrained grains [Parker and Klingeman, 1982; Wilcock and Southard, 1989]. In this study, a comparison of the initial and final surface grain-size distributions indicates that the proportion of sediment  $< 4$  mm ( $\approx D_{b25}$ ) declined by an average of 61% over the duration of the experiments.

In terms of the measured surface topography, Figure 4a indicates that water-working increased the range and standard deviation, broadened and flattened the peak, and transformed the shape from negatively skewed to positively skewed such that the PDFs of bed elevations for the equilibrium beds shared many of the characteristics of naturally worked river gravels [Nikora et al., 1998; Smart et al., 2004; Hodge et al., 2009b; Coleman et al., 2011]. However, inspection of the measured DEMs (Figure 3) indicates two scales of adjustment: the grain scale (due to surface coarsening and particle alignment) and the mesoscale (due to the development of patches of higher and lower bed elevation). Separation of the measured bed topography into surfaces representative of the grain and mesoscale topography using the technique of RRS highlights the fact that the changes in the frequency distributions of measured bed elevations were driven by grain-scale adjustments of surface topography (Figure 11).

Several workers have noted the contrast in surface skewness between screeded and water-worked beds and have attributed this difference to the development of an armor layer and the infilling of depressions in the bed surface by fines, which act to reduce the magnitude of surface elevation deviations below the mean bed level [Smart et al., 2004; Aberle and Nikora, 2006; Mao et al., 2011]. Such arguments, however, are difficult to reconcile with the observation in this study that the tails on the left of the grain-scale bed elevation PDFs for the water-worked beds are generally of similar length to, and fatter than, those for the screeded beds (Figure 11e). In these experiments, the development of positive skewness and the increased range of bed elevations are associated with the extension and fattening of the right-hand tail of the grain-scale bed elevation PDFs. Inspection of the grain-scale surfaces (e.g., Figures 11b and 11c) suggests that this can be attributed to the increased protrusion of coarser grains above the average bed level which may reflect the inability of large grains, once entrained, to be reincorporated into the bed [see also Mao et al., 2011] or the exhumation of particles in situ. The latter may result either from the movement of surrounding smaller grains or by a kinematic sorting effect whereby larger particles rise to the surface under the influence of transport-associated vibrations [cf. Rosato et al., 1987].

Previous workers have also reported positive correlations between the standard deviation of water-worked bed elevations and the surface grain size, suggesting that  $s$ ,  $D_{s50}$ , and  $D_{s84}$  may be used interchangeably as measures of surface roughness [Aberle and Nikora, 2006; Coleman et al., 2011; Brasington et al., 2012; Curran and Waters, 2014]. In this study, the scaling of particle size with estimates of  $s_g$  for the final surfaces in each experiment conforms, in general, to previously published field and laboratory gravel-bed data [e.g., Coleman et al., 2011].

The directional variograms for the experimental surfaces (Figures 6 and 12) conform to the pattern that has been observed in other studies of gravel-bed roughness and can be divided into scaling, transition, and saturation regions. As expected for screeded beds, estimates of  $h_{1x}$ ,  $h_{1y}$ , and  $H_x$  and  $H_y$  indicate that the surfaces at the start of each experiment had a roughness scale that equated to the size of the surface grains; was isotropic; and characteristic of a random process. The final beds were characterized by increases in  $\gamma$ ,  $h_1$ , and  $H$  in both downstream and cross-stream directions, reflecting an increase in surface roughness, roughness length, and increasing positive autocorrelation, respectively. The increases in  $\gamma$  and  $h_1$  can be attributed to the increase in surface grain-size associated with the development of the armor layer, and the increase in

$H$  can be explained by the fact that sequences of heights across a surface are less variable when the surface comprises fewer, larger particles.

Interestingly,  $h_{1x} \approx h_{1y}$  and  $H_x \approx H_y$  also characterized the water-worked beds which suggests that the scaling region isotropy of the initial surfaces was maintained for the duration of the experiments, despite surface coarsening. However, it is evident from the 2-D variograms (Figures 8b, 8c, and 12c) that the surface isotropy was only maintained for the lower part of the scaling region ( $< \sim 4$  mm), and that at longer distances, the water-worked surfaces became anisotropic ( $(h_x, 0) < (0, h_y)$ ). Such patterns of anisotropy are consistent with the preferential orientation of individual grains whereby grains are aligned with their  $a$  axes parallel to the flow. This finding stands in contrast to the argument that the longest axes of particles within active surfaces tend to be aligned transverse to the flow since this alignment facilitates particle movement by rolling around  $b$  and  $c$  axes [Aberle and Nikora, 2006]. Under this scenario,  $(h_x, 0) > (h_y, 0)$ , and grain-scale contours in isopleth maps of the 2-D variogram would be orientated transverse to the flow [e.g., Nikora and Walsh, 2004]. Such patterns, however, were not observed in our experiments, even during the early stages of the experiments when transport rates were high (Figures 8b and 12c). Several workers have suggested that flow-parallel particle alignments are, in fact, characteristic of surfaces experiencing very low transport rates or those formed as static armors [Butler et al., 2001; Aberle and Nikora, 2006; Curran and Waters, 2014]. Others, however, have found flow-parallel particle alignments to be characteristic of both mobile and static armors [Mao et al., 2011] and of actively aggrading surfaces [Cooper and Tait, 2009]. In the light of the above, it is clear that the azimuthal orientation of the  $a$  axes of fluvial gravels cannot be taken as a reliable indicator of either flow orientation or surface-forming mechanisms. This undoubtedly reflects the fact that  $a$  axis orientation is subject to multiple controls including, for example, flow direction, flow rate, particle size and shape, and underlying bed topography [Millane et al., 2006]. The difficulty of using particle orientation to reconstruct flow history is widely recognized in the sedimentological literature, which reports a wide range of particle orientation-flow direction relationships [e.g., Pettijohn, 1975, p. 69].

At longer distances, a comparison of the variograms shown in Figure 6a indicates that the water-worked beds are associated with longer correlation lengths than the screeded beds and, therefore, larger-scale bed features. The elliptical contours of the 2-D variograms (Figures 8b, 8c, and 12d) indicate that these structures are also flow aligned and are attributed to the organization of the bed into areas of higher and lower bed elevations with downstream and cross-stream length scales of  $\sim 200$  and 100 mm, respectively. There is no evidence for transversely orientated, multiparticle structures, as observed by Mao et al. [2011].

The area ratio (Figure 9) and inclination index (Figure 10) provide further insight into the characteristics of water-worked gravel beds but at contrasting scales. Values of  $A_R$  calculated at a grid resolution of 60 mm describe the bed at the mesoscale ( $\sim 180$  mm). At this scale, all surfaces were relatively flat ( $A_R \approx 1$ ). The water-worked surfaces, however, were associated with higher  $A_R$  values than screeded surfaces indicating greater surface complexity. This is attributed to the development of a mesoscale topography during the experiments. The inclination index was calculated at a DEM resolution of 0.15 mm and identified grain-scale structural differences between the screeded and water-worked beds. At the start of the experiment, the number of downstream and upstream facing inclinations for the screeded beds were approximately equal ( $I \approx 0$ ), indicating the random orientation of grains. At the end of each experiment, however, negative facing inclinations (upstream facing slopes) predominated ( $I < 0$ ) indicating the presence of grain imbrication. Little difference is observed between  $I$  and  $I_g$ . Values of  $I_m$ , however, vary erratically about zero suggesting that the mesoscale forms exhibit no preferred orientation in the  $xz$  plane.

#### 4.2. Evolution of Bed Surface Character

A novel aspect of this study was the high frequency of bed character measurement which reveals for the first time that the structural characteristics of mobile armors are preserved during sustained periods of sediment transport. As shown by the temporal evolution in the PDFs of bed elevations (Figures 4a and 5a–5c), directional variograms (Figures 6a, 7a, and 7b), 2-D variograms (Figures 8a–8c), area ratio, and inclination statistics (Figures 9 and 10b), each experiment commenced with a short period of rapid sediment structuring during which the screeded beds adjusted to the imposition of sediment transport. Thereafter, however, the structural character of the water-worked beds changed very little. Interestingly, the evolution in bed structure at grain and mesoscales occurred in tandem (compare patterns of particle alignment (Figures 8 and 12c) and imbrication (Figure 10b) and the emergence of the mesoscale topography (Figures 3, 9a, 12b, and 12d) and was tracked



by changes in surface grain size (Figure 2b). The time variation in the evolution of bed surface character undoubtedly reflected the decline in transport rates over the duration of each experiment which itself was a function of the feedback between the structural and textural development of the bed and the mobility of its constituent particles.

#### 4.3. Effect of Flow Strength on Bed Surface Character

A comparison of the final experimental surfaces reveals the influence of flow strength on bed surface character. In general, relatively little difference was observed in the structural character of the beds generated at the intermediate and highest flow strengths (e2 and e3, respectively). For example, the bed elevation PDFs and variograms have similar shapes (Figures 4b and 6b), and the values of bed elevation standard deviation ( $s$ ; Figure 5d), roughness length ( $h_1$ ; Figure 7c), Hurst exponent ( $H$ , Figure 7d), area ratio ( $A_R$ ; Figure 9), and inclination index ( $I$ ; Figure 10) are broadly comparable. In contrast, the equilibrium surface developed at the lowest flow strength (e1) was associated with a narrower and more peaked bed elevation PDF and lower values of  $s$ ,  $h_1$ , and  $H$  and  $A_R$  signifying a smoother, less irregular surface. This may, in part, reflect the lack of topographic development at the lowest transport rates (compare Figures 3g–3i).

Because surface grain size is a significant control on bed structure [Hodge *et al.*, 2009b; Mao *et al.*, 2011] some of the grain-scale differences in equilibrium bed structure identified in this study can be explained by the contrasts in surface armoring. As shown in Figure 7, for example, the adjustments of the length scales ( $h_1$ ) and the corresponding Hurst exponents ( $H$ ) with time (Figures 7a and 7b) and with flow strength (Figures 7c and 7d) are consistent with the corresponding adjustments of bed surface grain size shown in Figure 2c. In this context, it is interesting to note that the upper limit of  $h_1$  in both downstream and cross-stream directions for all water-worked surfaces may be approximated by  $h_1/D_{s50} \approx 0.85$  and that for the grain-scale surfaces by  $h_{rg} \approx D_{s84}$ . The similarity of  $H$  between e2 and e3 is consistent with the observation of Mao *et al.* [2011] that mobile armors generated at different shear stresses differ little in their complexity and stands in contrast with the reduction in surface complexity that is observed when static armors develop at progressively higher discharges [Aberle and Nikora, 2006; Mao *et al.*, 2011; Curran and Waters, 2014]. Interestingly, Mao *et al.* [2011] further report that the proportion of steep slopes measured at subgrain scales increased with discharge during mobile armor formation. In this study, however, the inclination indices of the equilibrium surfaces were similar, indicating that particle inclinations were independent of flow strength.

Close inspection of the directional variograms (Figure 6) indicates that the downstream correlation lengths ( $h_2$ ) of the water-worked beds greatly exceeded the size of the coarsest size fraction comprising the bed, indicating the presence of a larger-scale bed structure. Mao *et al.* [2011] quantified the correlation length scales of a number of equilibrium mobile armors and attributed a positive relationship with flow strength to the mobilization of coarser grains and the progressive development and growth of bed forms. In this study, a larger-scale bed structure characterized by distinct areas of higher and lower bed elevations, tens to hundreds of millimeter in scale, is evident in the DEMs of the water-worked surfaces (Figure 3). Development of this topography extended the range of the bed elevation PDFs (Figures 4 and 11d) and increased surface anisotropy (Figure 8c) and the area ratio measure of surface rugosity (Figure 9a). Inspection of DEMs, bed elevation PDFs, and area ratio statistics for the equilibrium surfaces suggests that this scale of bed structure increased significantly between e1 and e2 but only modestly between e2 and e3. This may reflect the fact that differences in transport rate were greater between e1 and e2 than between e2 and e3 (Figure 2a). We cannot fully explain this, but it may indicate that the sediment recirculation protocol affected sediment resupply (section 3.1). In particular, the discrete nature of sediment reintroduction may have introduced a sediment supply limitation that acted to constrain the bed load dynamic and the associated bed surface response.

Our observations that bed structure develops rapidly and that the role of flow strength is somewhat muted imply that modest flows ( $\tau^* \approx 0.03$ ) are capable of quickly achieving naturalized bed material conditions and that more energetic flows ( $\tau^* \approx 0.045$ ) produce only modest additional adjustments of the sedimentary fabric. If substantiated by further work, this is significant for experimentalists, because it indicates that although it is often necessary to start experimental runs with a screeded bed, grain reorganization is reasonably rapid and bed material fabric approaches “natural” within a short period. Providing experimental runs are long enough, results can be considered adequately free from contingent quirks that might arise from artificial starting

conditions. There are also implications at field scales in the context of river restoration practices that involve remodeling the river bed or gravel augmentation. Our results suggest that near-natural bed material fabrics and armor development can require only a few flows with the power to mobilize bed material in order to achieve near-natural conditions. This has significance for river ecology, where a concern of river managers is the rate at which benthic habitat is adequately restored in order to secure ecosystem functions.

## 5. Conclusions

Laboratory flume experiments were conducted to examine the evolution of bed surface structure in mobile armors formed at different bed load transport intensities. DEMs of the evolving surfaces were analyzed at grain and mesoscales using the distribution of bed surface elevations, the semivariance of the surface elevation structure, grain orientation, and values of the area ratio calculated at different DEM resolutions. The principle conclusions of the study are as follows:

1. Equilibrium mobile armors develop rapidly with the onset of sediment transport, with adjustments in both surface texture and structure proceeding in tandem. Previous studies of mobile armor layer development have focussed on the interpretation of equilibrium grain-size distributions. The results of this paper highlight the remarkable consistency in the metrics of mobile armor structure over prolonged periods of near-constant transport and demonstrate that mobile armors can also be characterized in terms of an equilibrium bed structure.
2. The equilibrium bed structure formed in each experiment exhibited two definable components: (a) a grain-scale component characterized by a positively skewed distribution of bed elevations, positive autocorrelation, an alignment in the direction of flow, and a predominance of upstream facing slopes and (b) a larger, mesoscale component which is also flow-aligned but that also displays a near-symmetrical distribution of bed elevations and a balance between upstream and downstream facing slopes. The former reflects the development of a coarse surface layer and the arrangement of particles therein, while the latter is attributed to the organization of the bed into areas of higher and lower bed elevations that show a tendency to be flow aligned.
3. Across a range of flows ( $0.023 \leq \tau^* \leq 0.047$ ), significant differences in the structural metrics of equilibrium surfaces were only apparent for  $\tau^* \leq \sim 0.03$ , with little difference at higher flows. In contrast to the findings of Mao *et al.* [2011], this implies that bed load transport rate is an important determinant of structural development when rates are low but that it is not important at higher flow strengths. We recognize, however, that our method of sediment recirculation may have constrained sediment supply, limiting the range of transport rates and the associated bed surface response. We also note the narrow grading of our experimental mixture and that further work might explore the effect of mixture sorting on bed structure development through the use of a range of more poorly sorted sediment mixtures.
4. Through the application of a regional-residual separation technique, the paper has illustrated the importance of isolating different scales of topographic variation when interpreting surface metrics for nonplanar surfaces. Further work, however, is needed to develop better techniques to identify and characterize the contribution of multiparticle structures to gravel-bed roughness. Further work is also needed to study the properties of structured beds in relation to their influence on the near-bed flow regime, particle stability, and transport rate. This will require the frequent and concurrent collection of spatially distributed measurements of bed microtopography, near-bed flow, and sediment transport.

### Acknowledgments

This research was supported by the Natural Environment Research Council of the UK through NE/H020772/1 (awarded to Powell) and NE/H020993/1 (awarded to Rice). The digital elevation models analyzed in this study are archived at the University of Leicester and are freely available from the lead author upon request. We are grateful to Judy Haschenburger, John Pitlick, and Tom Lisle for sharing particle size distributions from gravel-bed rivers in New Zealand and the USA and acknowledge the constructive comments of two anonymous reviewers, the Associate Editor, and Editor (John Buffington). Kerry Allen of the University of Leicester produced the figures.

### References

- Aberle, J., and V. Nikora (2006), Statistical properties of armoured gravel-bed surfaces, *Water Resour. Res.*, *42*, W11414, doi:10.1029/2005WR004674.
- Bathurst, J. C. (1993), Flow resistance through the channel network, in *Channel Network Hydrology*, edited by K. Bevan and M. J. Kirkby, pp. 69–98, John Wiley, Chichester.
- Bergeron, N. E. (1996), Scale-space analysis of stream bed roughness in coarse gravel-bed streams, *Math. Geol.*, *27*, 537–561, doi:10.1007/BF02066100.
- Bertin, S., and H. Freidrich (2014), Measurement of gravel-bed topography: Evaluation study applying statistical roughness analysis, *J. Hydraul. Eng.*, *140*, 269–279, doi:10.1061/(ASCE)HY.1943-7900.0000823.
- Brasington, J., D. Vericat, and I. Rychkov (2012), Modeling river bed morphology, roughness, and surface sedimentology using high resolution terrestrial laser scanning, *Water Resour. Res.*, *48*, W11519, doi:10.1029/2012WR012223.
- Brayshaw, A. C. (1984), Characteristics and origins of cluster bedforms in coarse-grained channels, in *Sedimentology of Gravels and Conglomerates*, *Can. Soc. Pet. Geol. Mem.*, vol. 10, edited by E. H. Koster and R. J. Steel, pp. 77–85, Can. Soc. of Petrol. Geol., Calgary.

- Buffington, J. M., and D. R. Montgomery (1997), A systematic analysis of eight decades of incipient motion studies, with special reference to gravel-bedded rivers, *Water Resour. Res.*, *33*, 1993–2029, doi:10.1029/96WR03190.
- Bunte, K., and S. R. Abt (2001), Sampling surface and subsurface particle-size distributions in wadable gravel- and cobble-bed streams for analyses in sediment transport, hydraulics, and streambed monitoring Gen. Tech. Rep. RMRS-GTR-74. 428 pp., U.S. Dep. of Agri., For. Serv., Rocky Mountain Research Station, Fort Collins, Colo.
- Butler, J. B., S. N. Lane, and J. H. Chandler (2001), Characterisation of the structure of river-bed gravels using two-dimensional fractal analysis, *Math. Geol.*, *33*, 301–330, doi:10.1023/A:1007686206695.
- Church, M., M. A. Hassan, and J. F. Wolcott (1998), Stabilizing, self-organized structures in gravel-bed stream channels: Field and experimental observations, *Water Resour. Res.*, *34*, 3169–3179, doi:10.1029/98WR00484.
- Clifford, N. J., A. Robert, and K. S. Richards (1992), Estimation of flow resistance in gravel-bed rivers: A physical explanation of the multiplier of roughness length, *Earth Surf. Processes Landforms*, *17*, 111–126, doi:10.1002/esp.3290170202.
- Coleman, S. E., V. I. Nikora, and J. Aberle (2011), Interpretation of alluvial beds through bed-elevation distribution moments, *Water Resour. Res.*, *47*, W11505, doi:10.1029/2011WR010672.
- Cooper, J. R., and S. J. Tait (2009), Water worked gravel beds in laboratory flumes—A natural analogue, *Earth Surf. Processes Landforms*, *34*, 384–397, doi:10.1002/esp.1743.
- Cooper, J. R., J. Aberle, K. Koll, S. J. McLelland, B. J. Murphy, S. J. Tait, and A. Marion (2008), Observation of the near-bed flow field over gravel bed surfaces with different roughness length scales paper presented at 4th International Association of Hydraulic Research River Flow Conference, Cesme-Izmir, Turkey.
- Curran, J. C., and L. Tan (2014), Effect of bed sand content on the turbulent flows associated with clusters on an armoured gravel bed surface, *J. Hydraul. Eng.*, *140*, 137–148, doi:10.1061/(ASCE)HY.1943-7900.0000810.
- Curran, J. C., and K. Waters (2014), The importance of bed sediment sand content for the structure of a static armour layer in a gravel bed river, *J. Geophys. Res. Earth Surf.*, *119*, 1484–1497, doi:10.1002/2014JF003143.
- Dietrich, W. E., J. W. Kirchner, H. Ikeda, and H. Iseya (1989), Sediment supply and the development of the coarse surface layer in gravel-bedded rivers, *Nature*, *340*, 215–217, doi:10.1038/340215a0.
- Ferguson, R. (2008), Gravel-bed rivers at the reach scale, in *Gravel-Bed Rivers VI*, edited by H. Habersack, H. Piegay, and M. Rinaldi, pp. 33–60, Elsevier, Amsterdam.
- Ferguson, R. I. (2012), River channel slope, flow resistance and gravel entrainment thresholds, *Water Resour. Res.*, *48*, W05517, doi:10.1029/2011WR0108850.
- Ferguson, R. I., M. Church, C. D. Rennie, and J. G. Venditti (2015), Reconstructing a sediment pulse: Modeling the effect of placer mining on Fraser River, Canada, *J. Geophys. Res. Earth Surf.*, *120*, 1436–1454, doi:10.1002/2015JF003491.
- Folk, R. L., and W. C. Ward (1957), Brazos River bar: A study of the significance of grain size parameters, *J. Sediment. Petrol.*, *27*, 3–26.
- Freund, R. J., and R. C. Littell (2000), *SAS® System for Regression*, 3rd ed., SAS Institute Inc, Cary, N. C.
- Gomez, B. (1995), Bedload transport and changing grain size distributions, in *Changing River Channels*, edited by A. Gurnell and G. Petts, pp. 177–199, John Wiley, Chichester.
- Grohmann, C. H. (2004), Morphometric analysis in geographic information systems: Applications of free software GRASS and R\*, *Comput. Geosci.*, *30*, 1055–1067, doi:10.1016/j.cageo.2004.08.002.
- Grohmann, C. H., M. J. Smith, and C. Riccomini (2011), Multiscale analysis of topographic surface roughness in the Midland Valley, Scotland, *IEEE Trans. Geosci. Remote Sens.*, *49*, 1200–1213, doi:10.1109/TGRS.2010.2053546.
- Hardy, R. J., J. L. Best, S. N. Lane, and P. E. Carbonneau (2010), Coherent flow structures in a depth-limited flow over a gravel surface: The influence of surface roughness, *J. Geophys. Res.*, *115*, F03006, doi:10.1029/2009JF001416.
- Hassan, M. A., and M. Church (2000), Experiments on surface structure and partial sediment transport on gravel bed, *Water Resour. Res.*, *36*, 1885–1895, doi:10.1029/2000WR900055.
- Hassan, M. A., and I. Reid (1990), The influence of microform bed roughness elements on flow and sediment transport in gravel bed rivers, *Earth Surf. Processes Landforms*, *15*, 739–750, doi:10.1002/esp.3290150807.
- Haynes, H., and G. Pender (2007), Stress history effects on graded bed stability, *J. Hydraul. Eng.*, *33*, 343–349, doi:10.1061/(ASCE)0733-9429(2007)133:4(343).
- Hillier, J. K., and M. Smith (2008), Residual relief separation: Digital elevation model enhancement for geomorphological mapping, *Earth Surf. Processes Landforms*, *33*, 2266–2276, doi:10.1002/esp.1659.
- Hobson, R. D. (1972), Surface roughness in topography: A quantitative approach, in *Spatial Analysis in Geomorphology*, edited by R. J. Chorley, pp. 221–246, Methuen, Mass.
- Hodge, R. A., J. Brasington, and K. Richards (2009a), In situ characterisation of grain-scale fluvial morphology using terrestrial laser scanning, *Earth Surf. Processes Landforms*, *34*, 954–968, doi:10.1002/esp.1780.
- Hodge, R. A., D. A. Sear, and J. Leyland (2013), Spatial variations in surface sediment structure in riffle-pool sequences: A preliminary test of the Differential Sediment Entrainment Hypothesis (DSEH), *Earth Surf. Processes Landforms*, *38*, 449–465, doi:10.1002/esp.3290.
- Hodge, R., J. Brasington, and K. Richards (2009b), Analysing laser-scanned digital terrain models of gravel bed surfaces: Linking morphology to sediment transport processes and hydraulics, *Sedimentology*, *56*, 2024–2043, doi:10.1111/j.1365-3091.2009.01068.x.
- Horn, B. K. P. (1981), Hill-shading and the reflectance map, *Proc. IEEE*, *69*, 14–47.
- Johansson, C. E. (1976), Structural studies of frictional sediments, *Geogr. Ann. Ser. A, Phys. Geogr.*, *58A*, 201–301, doi:10.2307/520535.
- Kirchner, J. W., W. E. Dietrich, F. Iseya, and H. Ikeda (1990), The variability of critical shear stress, friction angle, and grain protrusion in water worked sediments, *Sedimentology*, *37*, 647–672, doi:10.1111/j.1365-3091.1990.tb00627.x.
- Klinkenberg, B. (1994), A review of methods used to determine the fractal dimension of linear features, *Math. Geol.*, *26*, 23–46, doi:10.1007/BF02065874.
- Lacey, R. W. J., and A. G. Roy (2008), Fine-scale characterization of the turbulent shear layer of an instream pebble cluster, *J. Hydraul. Eng.*, *134*, 925–936, doi:10.1061/(ASCE)0733-9429(2008)134:7(925).
- Laronne, J. B., and M. A. Carson (1976), Interrelationships between bed morphology and bed-material transport for a small, gravel-bed channel, *Sedimentology*, *23*, 67–85, doi:10.1111/j.1365-3091.1976.tb00039.x.
- Mao, L. (2012), The effect of hydrographs on bedload transport and bed sediment spatial arrangement, *J. Geophys. Res.*, *117*, F03024, doi:10.1029/2012JF002428.
- Mao, L., J. R. Cooper, and L. E. Frostick (2011), Grain size and topographical differences between static and mobile armour layers, *Earth Surf. Processes Landforms*, *36*, 1321–1334, doi:10.1002/esp.2156.
- Marion, A., S. J. Tait, and I. K. McEwan (2003), Analysis of small-scale gravel bed topography during armouring, *Water Resour. Res.*, *39*, 1944–1973, doi:10.1029/2003WR002367.

- McLelland, S. (2013), Coherent secondary flows over a water-worked bed in a straight channel, in *Coherent Flow Structures at Earth's Surface*, edited by J. G. Venditti et al., pp. 275–288, Wiley, Chichester, doi:10.1002/9781118527221.ch18.
- McLelland, S. J., P. J. Ashworth, J. L. Best, and J. R. Livsey (1999), Turbulence and secondary flow over sediment stripes in weakly bimodal bed material, *J. Hydraul. Eng.*, *125*, 463–473.
- Millane, R. P., M. I. Weir, and G. M. Smart (2006), Automated analysis of imbrication and flow direction in alluvial sediments using laser-scan data, *J. Sediment. Res.*, *76*, 1049–1055, doi:10.2110/jsr.2006.098.
- Nikora, V. I., and J. Walsh (2004), Water-worked gravel surfaces: High-order structure functions at the particle scale, *Water Resour. Res.*, *40*, W12601, doi:10.1029/2004WR003346.
- Nikora, V. I., D. G. Goring, and B. J. F. Biggs (1998), On gravel-bed roughness characterization, *Water Resour. Res.*, *34*, 517–527, doi:10.1029/97WR02886.
- Ockelford, A., and H. Haynes (2013), The impact of stress history on bed structure, *Earth Surf. Processes Landforms*, *38*, 717–727, doi:10.1002/esp.3348.
- Oliver, M. A., and R. Webster (1986), Semi-variograms for modelling the spatial pattern of landform and soil properties, *Earth Surf. Processes Landforms*, *11*, 491–504, doi:10.1002/esp.3290110504.
- Papanicolaou, A. N., P. Diplas, C. L. Dancey, and M. Balakrishnan (2001), Surface roughness effects in near-bed turbulence: Implications to sediment entrainment, *J. Eng. Mech.*, *127*, 211–218, doi:10.1061/(ASCE)0733-9399(2001)127:3(211).
- Parker, G. (2006), The transport of gravel and sediment mixtures, in *Sedimentation Engineering: Processes, Measurements, Modeling and Practice*, edited by M. Garcia, pp. 165–251, Am. Soc. of Civil Eng., Virginia, doi:10.1061/40856(200)94.
- Parker, G., and P. C. Klingeman (1982), On why gravel bed streams are paved, *Water Resour. Res.*, *18*, 1409–1423, doi:10.1029/WR018i005p01409.
- Parker, G., C. M. Toro-Escobar, M. Ramey, and S. Beck (2003), Effect of floodwater extraction on mountain stream morphology, *J. Hydraul. Eng.*, *129*, 885–895, doi:10.1061/(ASCE)0733-9429(2003)129:11(885).
- Pender, G., T. B. Hoey, C. Fuller, and I. K. McEwan (2001), Selective bedload transport during the degradation of well sorted graded sediment bed, *J. Hydraul. Res.*, *39*, 269–277, doi:10.1080/00221680109499830.
- Petit, F., G. Houbrechts, A. Peeters, E. Hallot, J. V. Campenhout, and A. Denis (2015), Dimensionless critical shear stress in gravel-bed rivers, *Geomorphology*, *250*, 308–320, doi:10.1016/j.geomorph.2015.09.008.
- Pettijohn, F. J. (1975), *Sedimentary Rocks*, 3rd ed., Harper Row, London.
- Piedra, M. M., H. Haynes, and T. B. Hoey (2012), The spatial distribution of coarse surface grains and the stability of gravel river beds, *Sedimentology*, *59*, 1014–1029, doi:10.1111/j.1365-3091.2011.01290.x.
- Powell, D. M. (2014), Flow resistance in gravel-bed rivers: Progress in research, *Earth Sci. Rev.*, *136*, 301–338, doi:10.1016/j.earscirev.2014.06.001.
- Qin, J., D. Zhong, G. Wang, and S. L. Ng (2012), On characterization of the imbrication of armored gravel surfaces, *Geomorphology*, *159–160*, 116–124, doi:10.1016/j.geomorph.2012.03.012.
- Reid, I., L. E. Frostick, and A. C. Brayshaw (1992), Microform roughness elements and the selective entrainment and entrapment of particles in gravel-bed rivers, in *Dynamics of Gravel-Bed Rivers*, edited by P. Billi et al., pp. 253–266, John Wiley, Chichester.
- Robert, A. (1988), Statistical properties of sediment bed profiles in alluvial channels, *Math. Geol.*, *20*, 205–225, doi:10.1007/BF00890254.
- Robert, A. (1991), Fractal properties of simulated bed profiles in coarse-grained channels, *Math. Geol.*, *23*, 367–561, doi:10.1007/BF02065788.
- Rosato, A., K. J. Strandburg, F. Prinz, and R. H. Swendsen (1987), Why the Brazil nuts are on top: Size segregation of particulate matter by shaking, *Phys. Rev. Lett.*, *58*, 1038–1040, doi:10.1103/PhysRevLett.58.1038.
- Smart, G., J. Aberle, M. Duncan, and J. Walsh (2004), Measurement and analysis of alluvial bed roughness, *J. Hydraul. Res.*, *43*, 227–237, doi:10.1080/00221686.2004.9641191.
- Smith, P. L. (1979), Splines as a useful and convenient statistical tool, *Am. Stat.*, *33*, 57–62, doi:10.2307/2683222.
- Strom, K., A. N. Papanicolaou, N. Evangelopoulos, and M. Odeh (2004), Microforms in gravel-bed rivers: Formation, disintegration and effects on bedload transport, *J. Hydraul. Eng.*, *130*, 554–567, doi:10.1061/(ASCE)0733-9429(2004)130:6(554).
- Tan, L., and J. C. Curran (2012), Comparison of turbulent flows over clusters of varying density, *J. Hydraul. Eng.*, *138*, 1031–1044, doi:10.1061/(ASCE)HY.1943-7900.0000635.
- Wessel, P. (1998), An empirical method for optimal robust regional-residual separation of geophysical data, *Math. Geol.*, *30*, 391–407, doi:10.1023/A:1021744224009.
- Wilcock, P. R. (2001), The flow, the bed, and the transport: Interaction in flume and field, in *Gravel-Bed Rivers V*, edited by P. Mosley, pp. 183–219, New Zealand Hydrol. Soc., Wellington.
- Wilcock, P. R., and B. W. McArdeil (1993), Surface-based fractional transport rates: Mobilization thresholds and partial transport of a sand-gravel sediment, *Water Resour. Res.*, *29*, 1297–1312, doi:10.1029/92WR02748.
- Wilcock, P. R., and J. B. Southard (1989), Bedload transport of mixed size sediment: Fractional transport rates, bed forms, and the development of a coarse bed surface layer, *Water Resour. Res.*, *25*, 1629–1641, doi:10.1029/WR025i007p01629.
- Williams, G. P. (1970), Flume width and water depth effects in sediment-transport experiments U.S. Geol. Surv. Prof. Pap., 562-H.
- Wittenberg, L. (2002), Structural patterns in coarse gravel river beds: Typology, survey and assessment of the roles of grain size and river regime, *Geogr. Ann. Ser. A, Phys. Geogr.*, *84A*, 25–37, doi:10.1111/j.0435-3676.2002.00159.x.